Compressive mechanical properties of metal fiber sintered sheets at different strain rates

Ge Liu[a], Weidong Song[a,*], Peifeng Li[b]

[a] State Key Laboratory of Explosion Science and Technology, Beijing Institute of Technology, Beijing 100081, China

[b] School of Engineering, University of Glasgow, Glasgow G11 6BZ, UK

Abstract

The quasi-static and dynamic mechanical behaviors of metal fiber sintered sheets (MFSSs) with six relative densities and three fiber diameters at the strain rates ranging from 0.001/s to 2000/s are investigated by using Universal Materials Testing System and split Hopkinson pressure bar (SHPB) system. The effects of relative density, strain rate on the yield strength and the energy absorption efficiency of MFSSs are evaluated. Finite element models (FEM) based on computed tomography (CT) images and idealized fiber networks are developed to simulate the compressive behavior at different strain rates. The measured responses of MFSSs are generally in agreement with that predicted by the 3D reconstructed model and the idealized model. Two deformation modes of MFSSs are explored based on stress wave theory and a critical speed is calculated to differentiate the two modes. Finally, an idealized lapping network is proposed to explore the compatibility condition of the geometrical characteristics and the effect of the strain rate and relative density on the mechanical behavior MFSSs.

Keywords: strain rate effect; fiber network; compression; yield strength; deformation mode

1. Introduction

Bonded nonwoven random fiber network is ubiquitous around life. As a kind of bonded nonwoven random fiber network with large specific surface area, massive micro-size pore structures and adjustable porosity, MFSSs can be applied as catalyst support [1], filtering material [2] and noise reduction composite [3]. Besides that, with high specific stiffness and strength and good roughness, MFSSs also have a broad

* Corresponding author.
E-mail address: swdgh@bit.edu.cn (W. Song).

application in the field of cushioning and protection like car panels, roofing panels, structural filler and the core of sandwich panels. In these applications, random metal fiber sintered sheets are used to absorb energy under static and mostly dynamic loading usually in out-plane direction, also called through-thickness direction, to protect materials behind them. Under the circumstances, the research on the dynamic compressive behavior of MFSSs in out-plane direction is crucial to the design of the buffer structures containing MFSSs.

The mechanical properties of MFSSs are mainly dependent on raw material, sintering parameters and microstructures. Raw material controls the yield strength of MFSSs. For instance, MFSSs made from stainless steel have higher yield strength than that made from copper, if they have the same porosity and similar microstructures. Sintering parameters (sintering time and sintering temperature) have significant effect on the mechanical properties of MFSSs [4]. In the analysis of the relation between microstructures and mechanical performance, amounts of studies of MFSSs have been conducted experimentally, numerically and theoretically. It is widely accepted that the relative density governs the mechanical properties of MFSSs. The bond points formed between fibers [5], the length, the material properties of fibers [6, 7] and the residual strength of fibers [8] have a great effect on the feature of strain distribution in the fiber network and the strength of the fiber network. The nonlinear mechanical behavior during the bending of fibers determines the shape of the stress-strain curves of the fiber network [9]. The relative angle between fiber and the plane of sheet determines the fracture energy of MFSSs [10]. The MFSSs, in which fibers are approximately normal to the sheet plane, have higher fracture energy. The influence of bond failure and sliding between fibers on the macro-mechanical properties of fibrous material [11, 12] has been analyzed. Besides these conclusions drawn from quasi-static experiments, the influence of strain rate effect on the mechanical behaviors of MFSSs should also be noted. It has been proved that bending and buckling are main deformation modes under dynamic compressive loading and the material resists harder the deformation with the increasing of strain rates [13]. However, the dynamic loading also causes the temperature rise in MFSSs, which in some degree softens MFSSs [14]. In respect to energy absorption, MFSSs have better anti-penetration capability than metal plate when both of the

materials have the same areal density [15]. With the appearance of more sophisticated modeling and testing techniques, the contribution from microstructures to the macro-mechanical properties is discussed more and more frequently [16]. In addition, macroscopic phenomenological constitutive model [17], many microstructure-based theoretical constitutive models are introduced, such as models taking the geometry and the elasto-plastic behavior of fibers [18], the rotation, deformation, fracture of fibers and friction, fracture among fibers [19] and the dispersions of fibers [20] into account are developed to explain and predict the elasto-plastic behavior of MFSSs.

Although there are a variety of researches on the mechanical properties and deformation mechanism of MFSSs, the dynamic compressive mechanical response has been rarely studied. In the current paper, the compressive mechanical properties of MFSSs with different fiber diameters and relative densities were examined at different strain rates at normal temperature (298K). The relevance of the yield strength and the energy absorption efficiency of the MFSSs to the relative density and the strain rate was explored in detail. 3D reconstructed model and idealized random fiber network model were developed to predict the compressive strength of MFSSs. The structure of MFSSs was regularized into a lapping network model and the topological invariants of the structure were analyzed. The strain rate effect of MFSSs and the relation between the yield strength of MFSSs and the geometrical characteristics of structure were accounted for using this model.

2. Material and FEM

In this paper, the MFSSs are the product of Northwest Institute for Nonferrous Metal Research (China). The AISI 316L stainless steel bars are processed into fibers in three kinds of diameters (8μm, 12μm and 28μm) by bundle-drawing. Firstly, a certain amount of fibers with the same specifications are placed randomly in a mold by air-laid technology. By this means the distribution of fibers is uniform circumferentially [21]. Pressing this fiber deposit into a certain volume to ensure that the product will have a definite relative density. Relative density is equal to the ratio of the mass of MFSSs to the mass of 316L stainless steel with the same volume. Then, this fiber deposit together with the mold are put into a furnace and sintered by means of solid phase sintering in

vacuum at 10^{-2}Pa at temperature 1473K for an hour. The fiber deposit in the furnace is heated at a rate of 10K/min. When this sintered compact is finally cooled down to room temperature, a piece of metal fiber sintered sheet is manufactured.

The microstructures of MFSSs are characterized with the help of scanning electron microscope (SEM), Jeol-JSM 6460, as shown in Fig. 1 (a) (b). It can be confirmed that MFSSs are a kind of long fiber bonded nonwoven random fiber networks as Fig. 1 (a) shows, so the nature of the deformation of MFSSs bearing loading in out-plane direction is the bending and stretching of the fibers. The joints formed between two fibers are simplified as points and surrounding short curved beams. The simplification is shown in Fig. 1 (b) (c) (d).

An idealized stochastic fiber network model is developed based on three simplified assumptions: 1. Each bonding point is only related to two fibers, which intersect with each other. That is to say, there are only four lines intersecting with each other at each point in the idealized model and the joints are ignored. At these joints, many fibers intersect with each other as shown in Fig. 1(a) (b); 2. The torsion of the fibers will not occur; 3. The bonding points will not fracture. At the very beginning, n points, O_1, O_2,…, O_n, are generated in three-dimensional space randomly. Each point has a set of direction vectors O_n (<2> <4> <5> <7>) or O_n (<1> <3> <6> <8>), the number 1-8 means the quadrant of the vector as shown in Fig. 2 (c). The modulus of the vector is confirmed by Eq. (1):

$$\left|\mathrm{OP}\right| = \frac{r}{\cos\angle\theta} \tag{1}$$

where r is the radius of the circular cross-section of fiber. θ is the angle between the vector **OP** and z direction. There are four extra points for each center point O_i, [P_2 (O_i), P_4 (O_i), P_5 (O_i), P_7 (O_i)] or [P_1 (O_i), P_3 (O_i), P_6 (O_i), P_8 (O_i),]. For an arbitrary point P′ shown in Fig. 2 (c), another point P″ defined by center point O_2 can be found. The relationship between P′ and P″ must meet the conditions: the angle between vector **P′P″** and XY plane must be less than 5°. Under that condition, P″ should be the nearest point from P′. In this way, a piece of fiber between O_1 and O_2 can be represented by three line segments, namely O_1P', $P'P''$ and $P''O_2$ as shown in Fig. 2 (c). The length of this piece of fiber is defined as L. The equivalent length L is defined as follow:

$$\mathrm{L}=\left|\mathrm{O_1P'}\right|\sin\angle\theta_1+\left|\mathrm{P'P''}\right|+\left|\mathrm{O_2P''}\right|\sin\angle\theta_2 \tag{2}$$

where θ_1 is the angle between the vector $\mathbf{O_1P'}$ and z direction. θ_2 is the angle between the vector $\mathbf{O_2P''}$ and z direction. Controlling the volume of three-dimensional space V, the total length of the fibers ΣL will be obtained. The fiber parts out of the boundary are trimmed. We can calculate the current relative density ρ_r as follow:

$$\rho_r = \frac{\pi r^2 \sum L}{V} \tag{3}$$

where V is the volume of the confined space. If the value of ρ_r is given, the model can be generated as shown in Fig. 2 (a) (b). If the value is smaller or larger than the demand, the number of the center point O should be added or reduced, respectively.

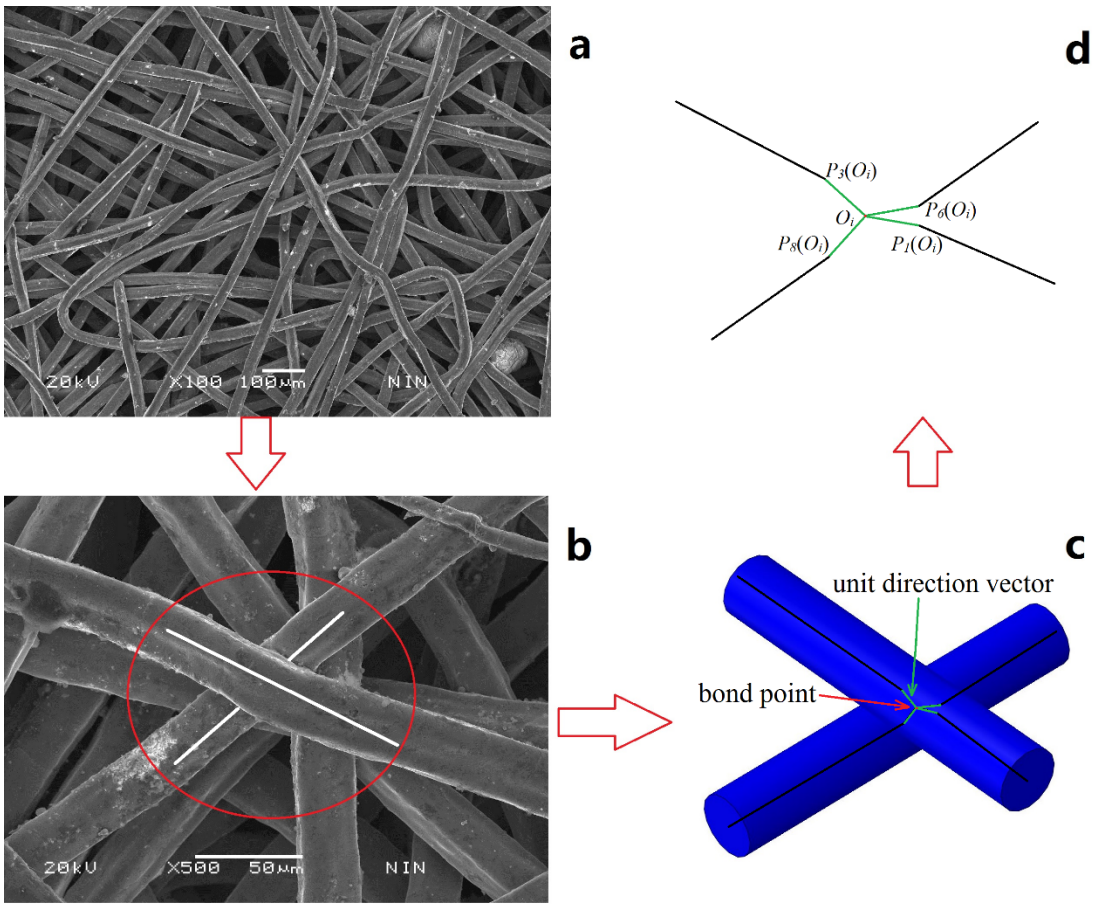

Fig. 1. The topology of MFSSs with 20% relative density and in 28µm fiber diameter in SEM (a) (b) and the simplification of the joint in red circle (b) (c) (d).

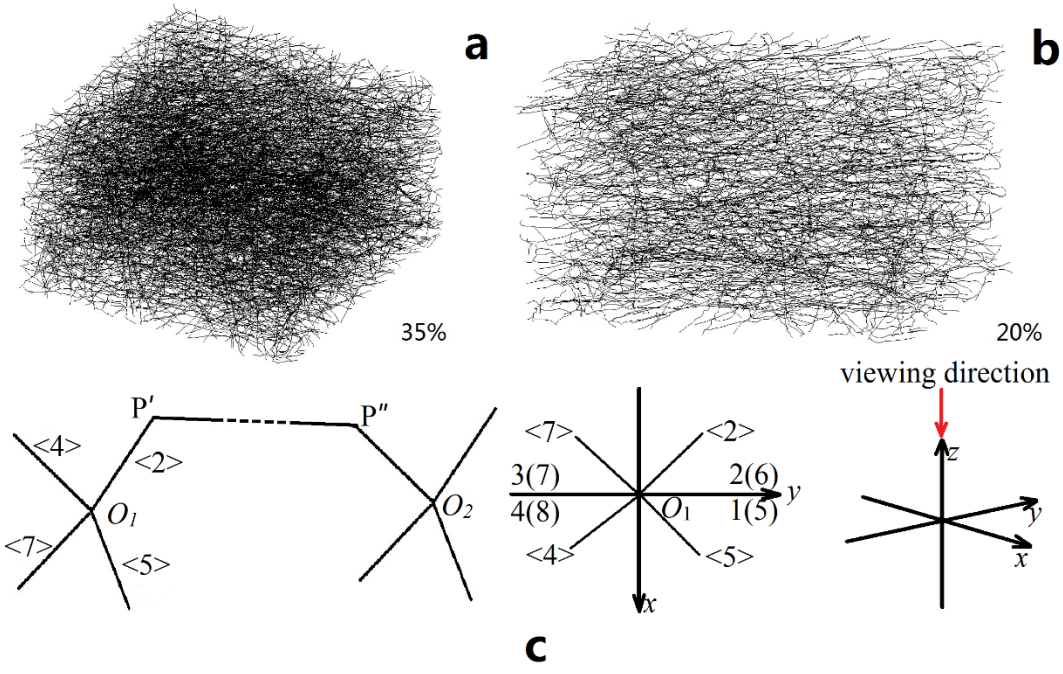

Fig. 2. Schematic of idealized stochastic network model. (a) model with 35% relative density; (b) model with 20% relative density; (c) simplified bonding point, coordinate system and quadrant.

Another kind of model is developed based on the μ-CT technology and 3D reconstruction method. MFSSs are scanned by a synchrotron radiation-based μ-CT with the resolution of 0.8μm and energy resolution of 5×10^{-3} in Shanghai Synchrotron Radiation Facility. The monochromator works at the photon energy range of 8-72.5keV. The voxel size is 3.25μm. By choosing an appropriate field, a model is reconstructed in this field by using MIMICS (kind of commercial software). At the same time the convergence and the calculation cost are taken into consideration. Discrete voxels will be removed with the usage of region growing and the cuspidal points on the fiber surface will be eliminated by smoothing. The 3D volume rendering model and final finite model are shown in Fig. 3.

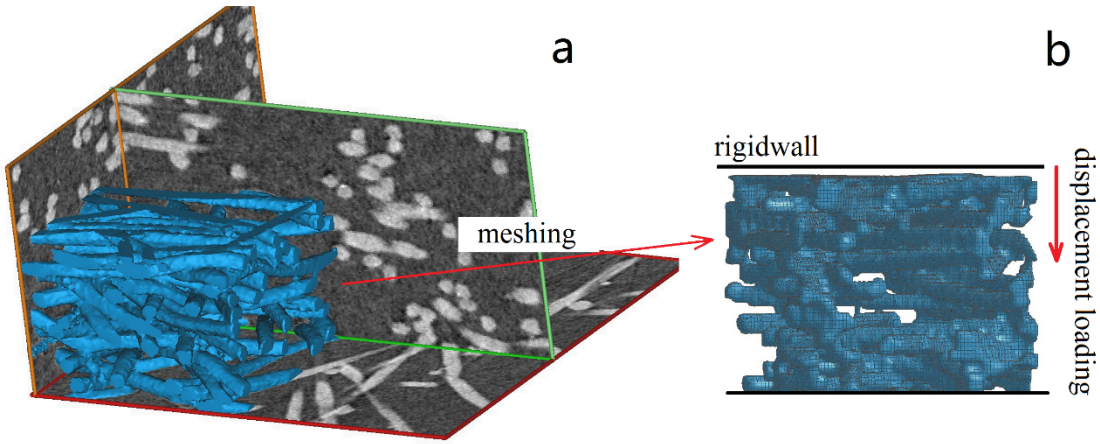

Fig. 3. The volume rendering model (a) and the finite model (b).

Numerical simulation is conducted by using software LS-DYNA. The impact load is applied by using rigidwall with a certain speed. For the 3D reconstructed model, the mesh type of the model is hexahedral mesh. For the idealized model, beam element is adopted due to the precision and the computing cost in numerical simulation. Free boundary condition and the general contact (a type of keywords) are used. Plastic kinematic (PK) model [22] is adopted and strain rate is accounted for using the Cowper and Symonds model [23]. The material parameters and the values of the variables of PK model are listed below:

Table 1. Material parameters and the variables of PK model. SI-unit system (kg-m-s)

Density	**Young's modulus**	**Poisson's ratio**	**Yield stress**	**Strain rate parameter *C***	**Strain rate parameter *P***
$7.93*10^3$	210	0.3	170	2	9

Because the grid size in CT reconstructed model depends on the voxel size (3.25μm*3.25μm*1μm), the SI-unit system is converted from kg-m-s to kt-μm-s in the numerical simulations. The side length of 8 nodes regular hexahedral constant stress solid element is 6.5μm. The beam elements use Belytschko-Schwer full cross-section integration, and 4*4 Gauss quadrature is used. The cross-section type is tubular. Considering the rate-dependent yield stress, the Cowper and Symonds model scales the yield stress with the factor:

$$1+\left(\frac{\dot{\varepsilon}}{C}\right)^{1/P} \tag{4}$$

P and C are the parameters of the scale factor given in Eq. 4. The parameters at strain rates 1/s and 10/s used to fit yield stress-strain rate curve are obtained from a research on the flow stress of AISI 316L at high strain rates [24].

3. Mechanical testing

3.1 Specimens

The specimens used in this paper are cut from several large pieces of MFSSs. Due to the local heterogeneity caused by production process, the stochastic distribution of fibers can't assure that the relative densities everywhere are same. The relative densities of specimens are not equal to each other, but the deviation is usually smaller than 2%. Thus, some specimens are collected in a group with the deviation of ±1% for the sake of analysis. There are five groups of specimens in fiber diameter (28μm) with different relative densities, namely, 20%±1%, 24%±1%, 26%±1%, 31%±1% and 37%±1% tested in the study. These five groups will be directly called 20%, 24%, 26%, 31% and 37% for simplicity in the following sections. Additional specimens in fiber diameter (8μm) with a relative density 41% and specimens in fiber diameter (12μm) with a relative density 25% are also used, because the effect of the fiber diameter on the dynamic mechanical behavior of MFSSs is not concerned in this paper. The specimens are cut into cylinder with the diameter of 10mm and the length of 10mm by wire-cutting electrical discharge machine as shown in Fig. 4.

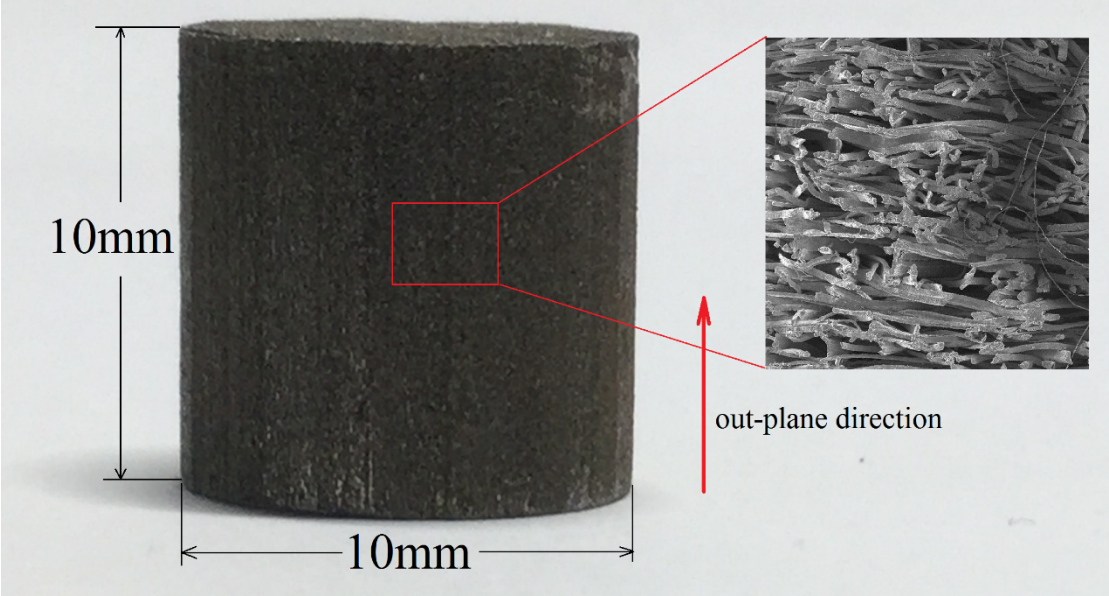

Fig. 4. The cylindrical specimen and its longitudinal section.

3.2 Experiments

WDW-300 electronic universal testing machine has been used to conduct uniaxial quasi-static compression tests on the specimens with relative densities 37% and 41% in fiber diameters (28μm and 8μm), respectively. The compressive process is controlled by displacement and the strain rate is set as $10^{-3}/s$. Loading direction is the out-plane direction as mentioned above. The nominal stress is the ratio of the reaction force to the initial area of the cross-section of the specimen, and the nominal strain is defined as the ratio of the displacement of crosshead to the initial height of the specimen. The dynamic load tests are performed with the usage of SHPB system as shown in Fig. 5. The length, the diameter and the Young's modulus of the steel Hopkinson Bar are 1m, 13mm and 200Gpa, respectively. The speed of the stress wave in both steel incident and transmission bars is 5050m/s. The length of the striker bar is 400mm. Dynamic strain measurement equipment is used to capture the signals from the resistance strain gauge on the incident bar and the signals from the semiconductor strain gauge on the transmission bar. The sampling frequency is 2.5MHz. The original data are processed by two-wave method with the usage of a program in MATLAB. Because for MFSSs the amplitudes of the incident wave and the reflected wave are similar with each other, so it would be better to use the signal from the semiconductor to determine the stress. The nominal stress and the nominal strain are calculated with the usage of the reflected

wave signal and the transmitted wave signal. The averaged curve of three or four replicate tests is adopted in this paper. It is important to note that here the nominal strain is only a macroscopic average value.

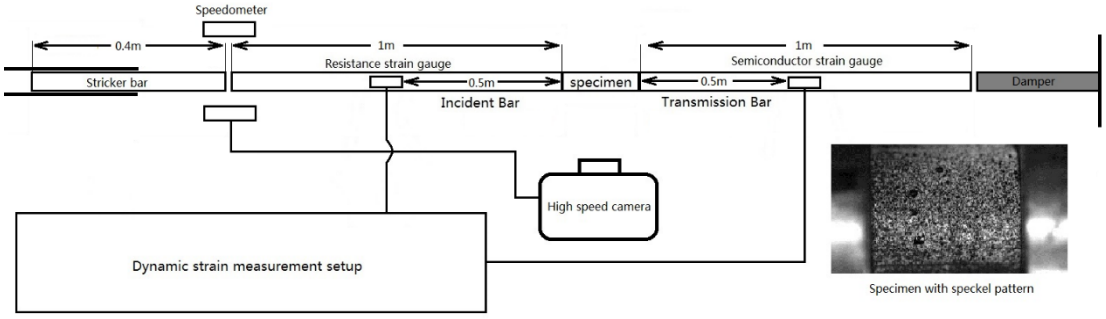

Fig. 5. The schematic of the split Hopkinson pressure bar system.

Table 2. Specimens for experiments.

Fiber diameter	**Relative density**	**Quasi-static 0.001/s**	**1100/s**	**1500/s**	**2000/s**
28μm	20%	√	√	-	-
	24%	√	√	-	√
	26%	√	√	-	-
	31%	√	√	-	-
	37%	√	√	√	-
8μm	41%	√	√	√	-
12μm	25%	-	√ (DIC)	-	-

"√" means the test has been done; "-" means these is no test for this item. "DIC" means the data of this item are analyzed by using Digital Image Correlation (DIC) technique.

4. Results and Discussion

4.1 Strain rate effect and Energy absorption property

The stress-strain curve directly output from MATLAB as shown in Fig. 6 must be processed further. Smoothing the piece of curve around the yield point weaken the effect of fluctuation, and the intersection of the smoothed line and the rising edge is defined as the yield point. The rising edge can't represent the elastic part in the stress-strain curve obtained from SHPB system, so it is cut off. Under the loading of 400mm striker bar, the strain can reach about 0.15. The energy absorption efficiency is

calculated by Eq. 5 [25], where ε_m and σ_m are the maximum strain corresponding to the calculation interval and the stress at this strain, respectively.

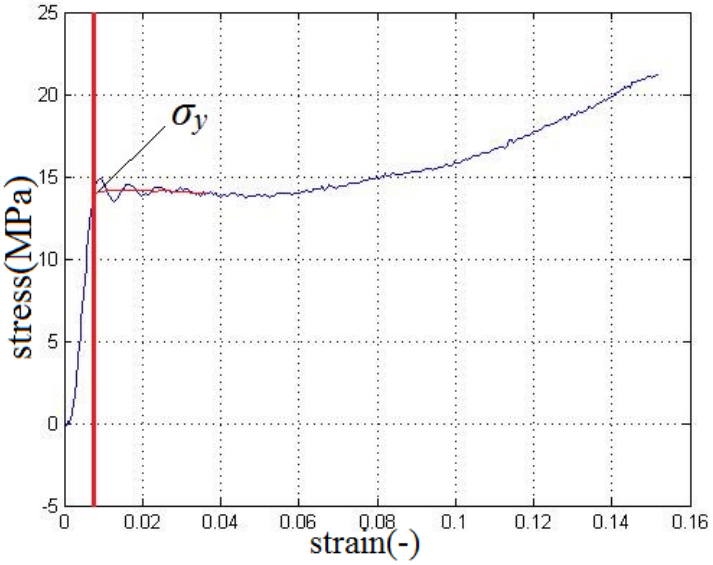

Fig. 6. The choice of yield point σ_y and the processing of the curve.

$$\eta = \frac{\int_0^{\varepsilon_m} \sigma d\varepsilon}{\sigma_m} \tag{5}$$

The effect of the relative density at a high strain rate and the effect of the strain rate on the yield strength are studied. The energy absorption efficiency under each condition is also analyzed accordingly. The experimental results show that the yield strength of MFSSs and the strain hardening rate increase with the increase of the relative densities. This increase is not linear especially for the relative densities varying from 20% to 24% and 31% to 37%. As it can be seen in Fig. 7 (a), the relative density is still a major influence factor for the mechanical behavior of MFSSs. Generally speaking, the energy absorption efficiency decreases slightly with increasing the relative densities as shown in Fig. 7 (b).

In Fig. 7 (c) (e), the yield strength increases with the increase of the strain rates. The raw material 316L stainless steel has the same strain rate effect. At the same time, there is no obvious transverse expansion under dynamic compression, until the strain reaches 0.3 as shown in Fig. 8. Fig. 7 (d) (f) show that the strain rates have no obvious influence

on the energy absorption efficiency. In a word, larger relative density and higher strain rate loading will enhance the yield stress of MFSSs, but they exert no obvious effect on the energy absorption efficiency of MFSSs.

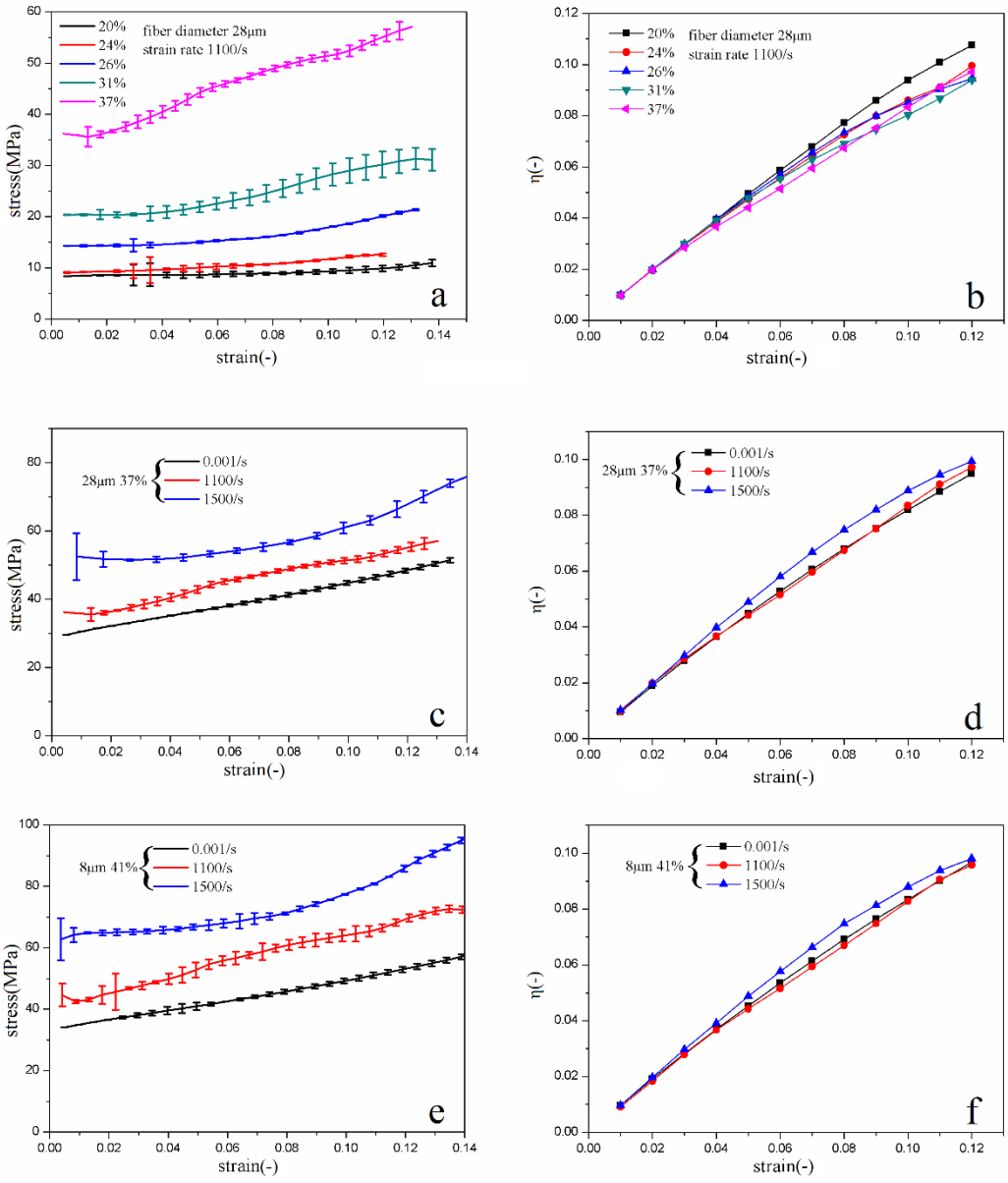

Fig. 7. Stress-strain curves and energy absorption efficiency η-strain curves: a. comparison among the stress-strain curves with different relative densities at strain rate 1100/s; b. the energy absorption efficiency corresponding to a; c. comparison among the stress-strain curves at different strain rates with fiber diameter 28μm and relative density 37%; d. the energy absorption efficiency

corresponding to c; e. comparison among the stress-strain curves at different strain rates with fiber diameter 8μm and relative density 41%; f. the energy absorption efficiency corresponding to e.

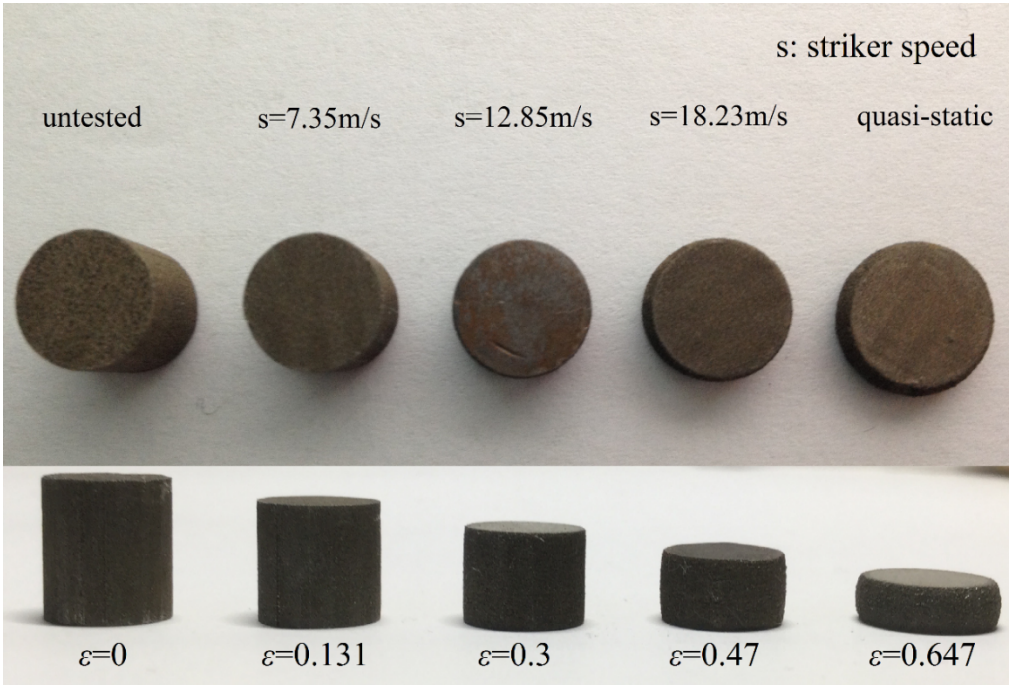

Fig. 8. The specimens from left to right are corresponding to untested, 7.35m/s striker speed, 12.85m/s striker speed, 18.23m/s striker speed and quasi-static loading.

4.2 Comparison between experimental and numerical results

Numerical results show almost the same trend compared with experimental results: the yield strength increases with the increase of the relative densities and strain rates. As it can be seen in Fig. 9(a), the numerical predictions from the idealized model agree well with the experimental results for MFSSs with lower relative densities and there is a discrepancy of 5MPa between the numerical predictions and the experimental results for MFSSs with higher relative densities. This phenomenon can be attributed to the differences between the modeling method of the idealized model and the internal morphology of MFSSs with high relative density. The modeling method is based on the simplified internal morphology of MFSSs with low relative density for example 20%. The majority of bonding point are formed by two fibers, but in MFSSs with high relative density for example 37%, bonding points locate next to each other and many bonding points come together forming a big rigid structure. Thus, the rigid structure

has higher strength than the idealized structure. That is why there is a discrepancy between numerical predictions and experimental results for high relative density. The comparison of these two types of morphology can be seen in Fig. A attached in the Appendix A. In addition, the yield strength and the strain hardening rate of numerical results are lower than those of the experimental results, because the bonding points are directly replaced by four bending beams in the idealized model. The deformation of the fiber around the bonding point, which is equivalent to the bending of a cantilever, is harder than the bending of a curved beam. The strain rate effect of MFSSs is also simulated with the usage of FEM model generated by 3D reconstruction technique and the idealized model as shown in Fig. 9(b). Both of these two models can predict the yield strength of MFSSs accurately. The results of FEM model agree better with the experimental results compared with the idealized model, because all microstructures and internal morphology are taken into consideration in 3D reconstruction. In the simulating process, it can be found that only some small regions of 3D model deform when the stress reaches the yield strength (red fields in Fig. 10). In contrast to this state, the densification stage almost begins when most of parts deform as shown in Fig. 10. No matter in which stage there is even no stress in some parts of the fibers (blue fields), which means that not all of the fibers in MFSSs contribute to the load bearing.

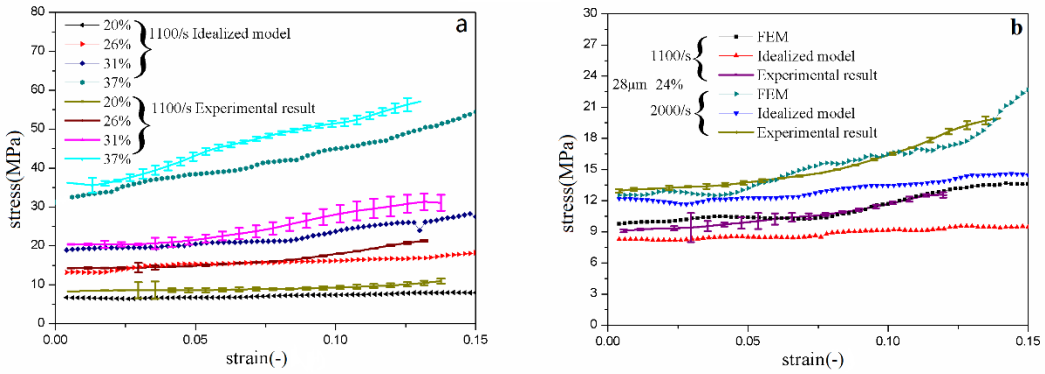

Fig. 9. Comparison between measured and simulated results: a. specimens and models with different relative densities at strain rate 1100/s; b. specimens and models at different strain rates with relative density 24%.

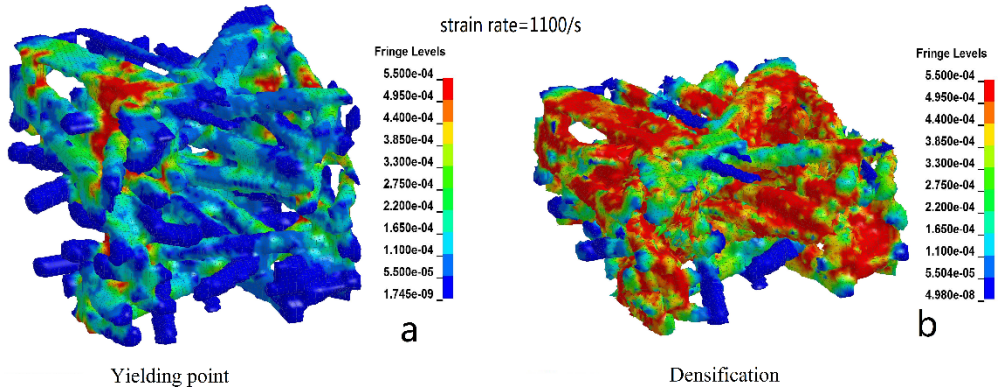

Fig. 10. Different von mises stress distributions (MPa) of FEM model in different stages.

4.3 Compatibility conditions of geometrical characteristics

According to the above-mentioned results, an assumption is proposed reasonably that the topological structure of MFSSs changes with the relative density. To verify this assumption and to study the relation between the microstructures and the yielding behavior of MFSSs under static and dynamic compressive load, MFSSs network is regularized in an idealized lapping network. With the help of this model, the compatibility conditions of the geometrical characteristics and the dependency between the geometrical characteristics and the yield strength of MFSSs are explored, respectively.

The arrangement mode of the fibers in the idealized lapping network shown in Fig. 11 is similar with a braided structure: the fibers in the adjacent layers are staggered in in-plane direction. These fibers are not woven together. They "expand" in the out-plane direction on the contrary. The azimuth of the fibers is simplified into 0º and 90º in the lapping network. Assuming that the height and the width of a part in the model are H and D, respectively. The number of the fibers in the layer with the width of D is n. The lapping network mainly refers to the geometrical characteristics θ, ρ_l and k. θ is the average pitch angle of the fibers. The geometrical characteristic ρ_l represents the ratio of the total projected length of the fibers per layer to the width of the corresponding layer. k is a coefficient characterizing the settlement or the warping of the fibers at the bonding point as shown in Fig. 12. The coefficient k is defined as follows:

$$k = \frac{\overline{OO'}}{d} \tag{6}$$

where d is the diameter of the fiber. $\overline{OO'}$ is the vertical distance between the projection of a horizontal center line O and the projection of an extended line. When a fiber settles at a bonding point, the value of k is less than 1. When a fiber warps, the value of k is greater than 1.

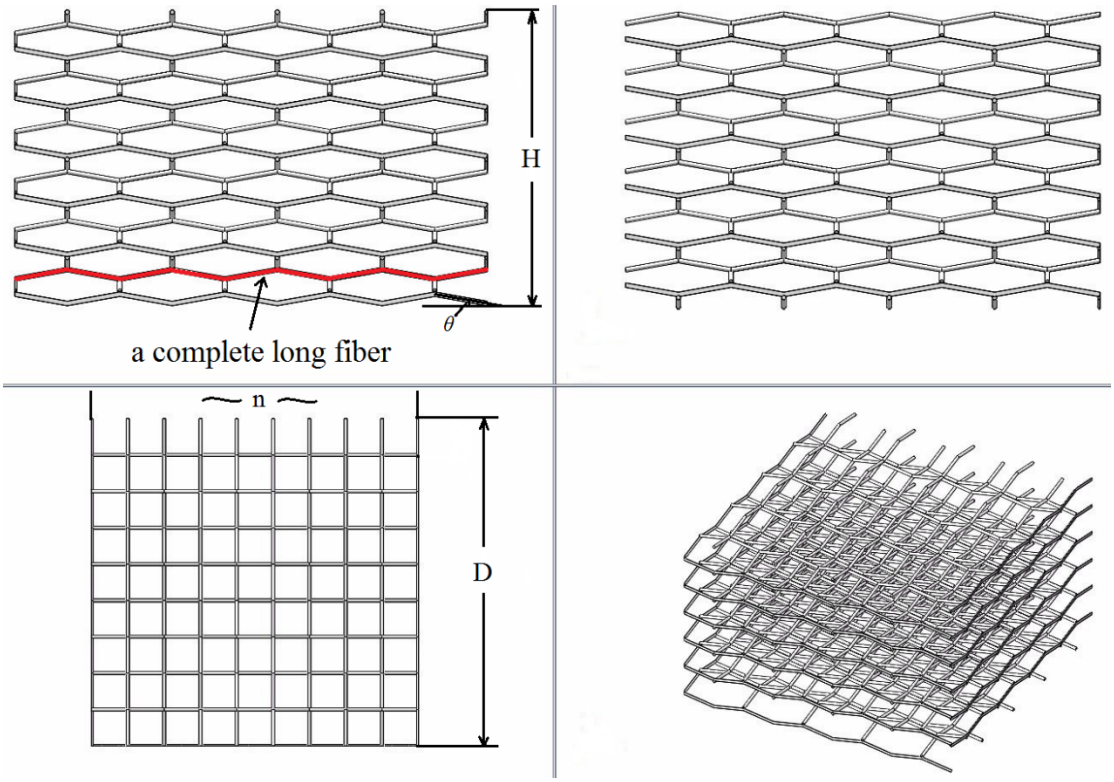

Fig. 11. The four views of the idealized lapping network: on the top left, top right, left below and right below are front view, left elevation, top view and 3D view, respectively.

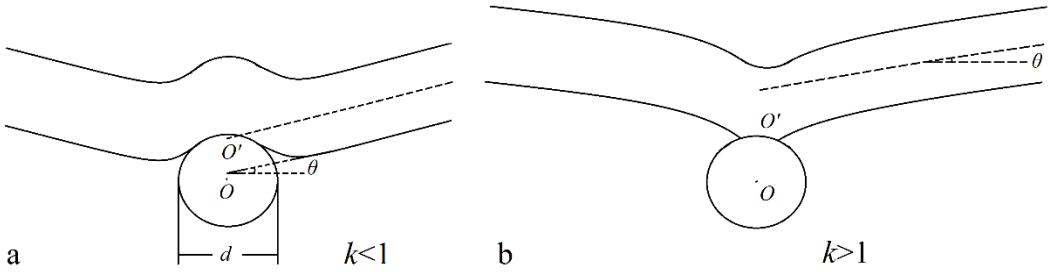

Fig. 12. The settlement (a: k<1) or the warping (b: k>1) of fiber at the bonding point.

Hence, some geometrical relationships can be built based on this model:

$$l' = \frac{D}{2n\cos\theta} = \frac{l}{2n} \Rightarrow l = \frac{D}{\cos\theta} \tag{7}$$

$$m = \frac{H}{\tan\theta \dfrac{D}{2n} + kd} \tag{8}$$

$$V_l = Al = \frac{\pi d^2}{4} l = \frac{\pi d^2 D}{4\cos\theta} \tag{9}$$

$$\rho_r = \frac{\sum V_l}{V_\Sigma} = \frac{mnV_l}{V_\Sigma} = \frac{nd}{D} \frac{\pi}{2\sin\theta \dfrac{D}{nd} + 4k\cos\theta} \tag{10}$$

$$k = \frac{1}{4\cos\theta} \left(\frac{nd}{D} \frac{\pi}{\rho_r} - 2\sin\theta \frac{D}{nd} \right) \tag{11}$$

where l' is the length of a fiber segment between two neighboring bonding points. Coefficient m is the number of the layers in out-plane direction. Coefficients l and V_l are the length and the volume of a single fiber and A is the area of the cross-section of the fiber. As one expression of the coefficient k, Eq. 11 is derived from Eq.10, which is the expression for the relative density of the model.

The value range of the pitch angle θ is also analyzed based on the CT images. On the one hand, as shown in Fig. 13 (a), the pitch angle θ mainly varies from 5º to 15º. On the other hand, with analyzing the area ratios of the cross-section of the fibers to the area of the cut-layer, a conclusion will be given that the area ratio at each cut-layer should be approximately equal to the relative density of the whole specimen. Actually, for an ideal stochastic structure, the relative density of each lamina should be equal to the relative density of the whole structure. Considering the heterogeneity of the material in reality, the relative density of each lamina varies over around the relative density of the specimen, which has been validated in Fig. 13 (b). For five arbitrary cut-layers, the relative densities of these five laminas given by MIMICS are 18.5%, 18.2%, 18%, 17.5% and 18.8%, respectively. The relative density of this specimen is 17.7%. When the width of the lamina is small enough, the fibers in the lamina are right circle cylinders or oblique circle cylinders. Because these cylinders have the same height, the relative density of the lamina is equal to the area ratio of the cross-section of the fibers to the area of the cut-layer. Therefore, the area ratio at each cut-layer is approximately equal to the relative density of the whole specimen. For the lapping network, the value of the

area ratios of the cut-layers should be Eq.11 (the normal direction of the cut-layer is not parallel and perpendicular to the extension direction of fibers).

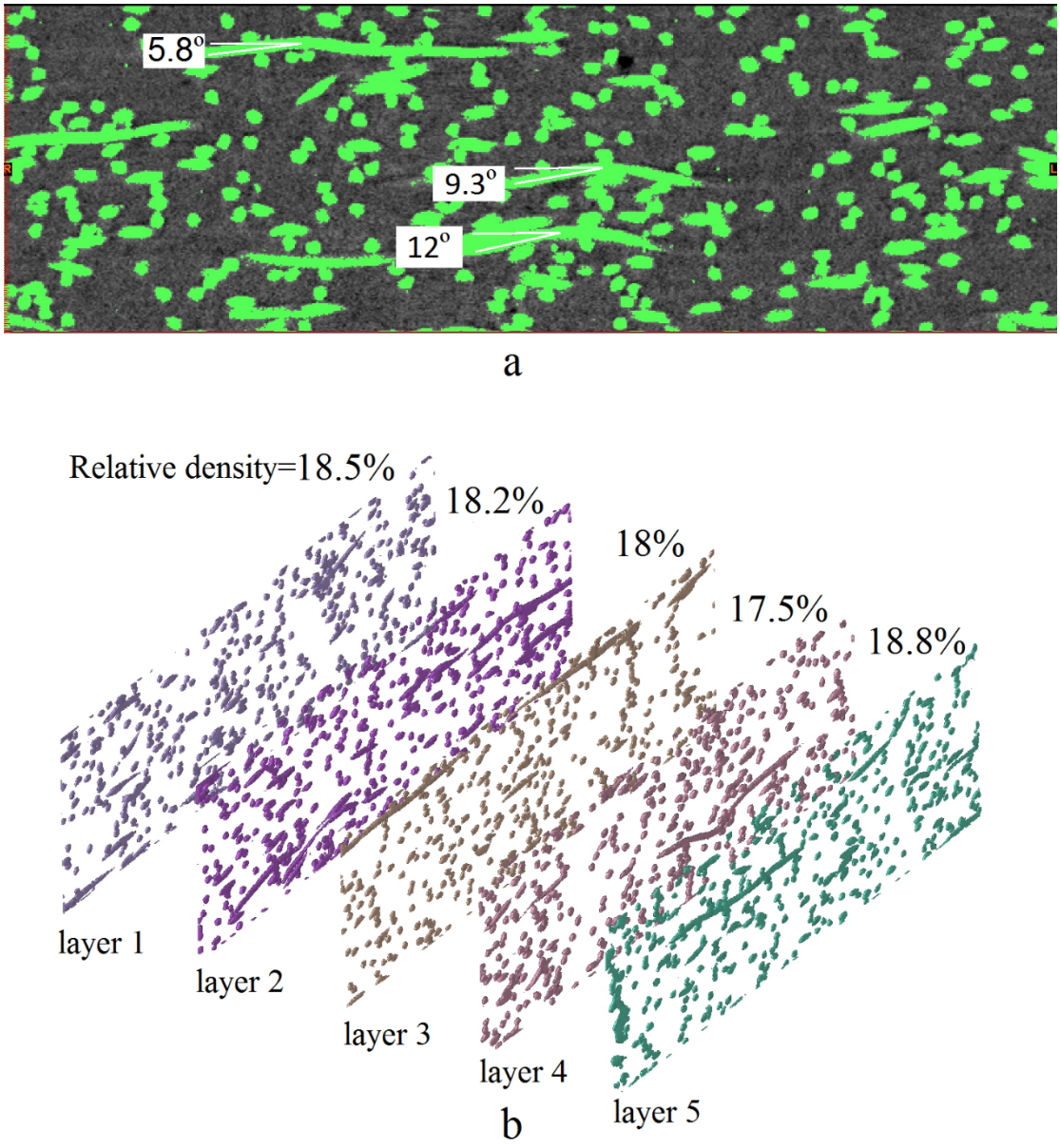

Fig. 13. The CT analysis results of MFSSs sample with the relative density of 17.7%: a. the pitch angles of fibers in MFSSs; b. the area ratios of fibers cross-sectional area to the area of cut-layer at the five sections.

Under compressive load, the bending deformation of the fibers plays an important role in the deformation of MFSSs. There should be a connection between the yield strength of the whole structure and the yielding of the fibers. From MFSSs to the lapping network, an assumption is introduced that all fibers deform and yield when the

structure deforms and yields, though it has been proved to be unreal based on the simulation results. According to the stress-strain curves of MFSSs, the deformation mode of the fibers should be bending dominant deformation (mode 2) in Fig. 14 (b), but not buckling (mode 1) in Fig. 14 (a). Buckling will result in a jump of the stress at yielding point, which is nonexistent in the stress-strain curves of MFSSs. Thus, by considering the bending of the fiber, the free-body diagram is shown in Fig. 14 (c). F is the component force of the total force applied on the top surface of the structure. l'' is half of l'. F_j is the reaction force from the symmetric part of the fiber. M is the bending moment at the bonding point. Because the numerical results mentioned above show that the structure has no obvious deformation when MFSSs yield, it can be reasonably assumed that the structure also has no obvious deformation when MFSSs yield in the experiments. In the lapping network, the structure yields when there is only a small increment of the vertical displacement of the fiber end at the slide bearing as shown in Fig. 14 (3). Based on the static balance condition and the deformation compatibility condition, Eq. 12 is obtained for the rectangular cross-section. Rewriting the Eq. 12, another expression of the coefficient k is given in Eq. 13. For the circular cross-section Eq. 14 is derived. The expression of K is given in Eq. 15. The detailed deducing is presented in Appendix B.

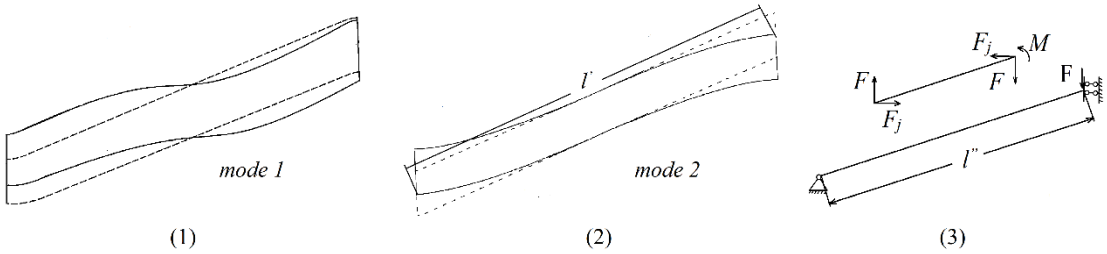

Fig. 14. The deformation mode and the free-body diagram of fibers under compressive load in the model. F is the component force of the total force applied on the top surface of the structure. l'' is half of l'. F_j is the reaction force from the symmetric part of the fiber. M is the bending moment at the bonding point.

$$\frac{\sigma_{y316L}}{\sigma_{yMFSS}}\left(\frac{nd}{D}\right)^3=\left[\frac{3\left(\cos\theta-K\sin\theta\right)}{k\pi\cos\theta}+\frac{nd}{D}\frac{4\left(\sin\theta+K\cos\theta\right)}{\pi}\right] \tag{12}$$

$$k = \frac{3\left(\cos\theta - K\sin\theta\right)}{\pi\cos\theta} \Bigg/ \left[\frac{\sigma_{y316L}}{\sigma_{yMFSS}}\left(\frac{nd}{D}\right)^3 - \frac{nd}{D}\frac{4\left(\sin\theta + K\cos\theta\right)}{\pi}\right] \tag{13}$$

$$\left[\frac{\sigma_{y316L}}{\sigma_{yMFSS}}\left(\frac{nd}{D}\right)^3 - \frac{nd}{D}\frac{4\left(\sin\theta + K\cos\theta\right)}{\pi}\right] = \frac{4\left(\cos\theta - K\sin\theta\right)}{\pi\cos\theta} \tag{14}$$

$$K = \left[1 - 3\left(\frac{nd}{D}\right)^2\cos^2\theta\right]\frac{\tan\theta}{\tan^2\theta + 3\left(\frac{nd}{D}\right)^2\cos^2\theta} \tag{15}$$

Based on the aforementioned discussion on the value range of the pitch angle θ, the solution curves are shown at the range from 5º to 15º. In terms of different relative densities, the solution curves corresponding to the cross-section type 1 and cross-section type 2 are very close to each other as shown in Fig. 15 (c). It should be noted that there are two lines in the solution domain. Only line 1 is the solution and line 2 is the intersecting line of a singular face of Eq. 13 and the solution face of Eq. 11 as shown in Fig. 15 (a). When the compatibility conditions of the geometrical characteristics are fixed, the coefficient k and nd/D are approximately two topological invariants as shown in Fig. 15 (d) and (e). It means that the state of the fiber at the bonding point and the density of the fibers per layer are determined. The two lines only fluctuate within a small range with the changes of the pitch angle, which indicates that when the pitch angle is small, the mechanical behavior of MFSSs is mainly dominated by the two topological invariants. The density of the fibers per layer is mainly dependent on the lay-up technology. The state of the fiber at bonding points depends on the method of the relative density control during processing.

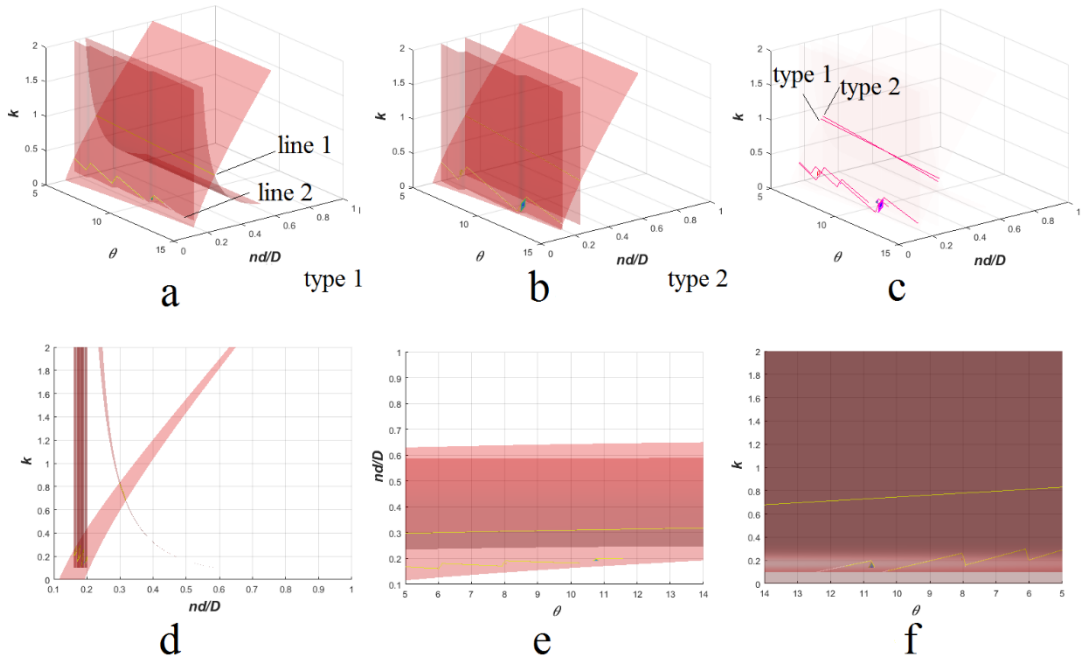

Fig. 15. The solution of the Eq. 11, Eq. 13 and Eq. 14. a. The solution of the Eq. 11 and Eq. 13. b. The solution of the Eq. 11 and Eq. 14. c. Comparison between the solutions considering two cross-section types. Figures d, e and f are the three views of figure a.

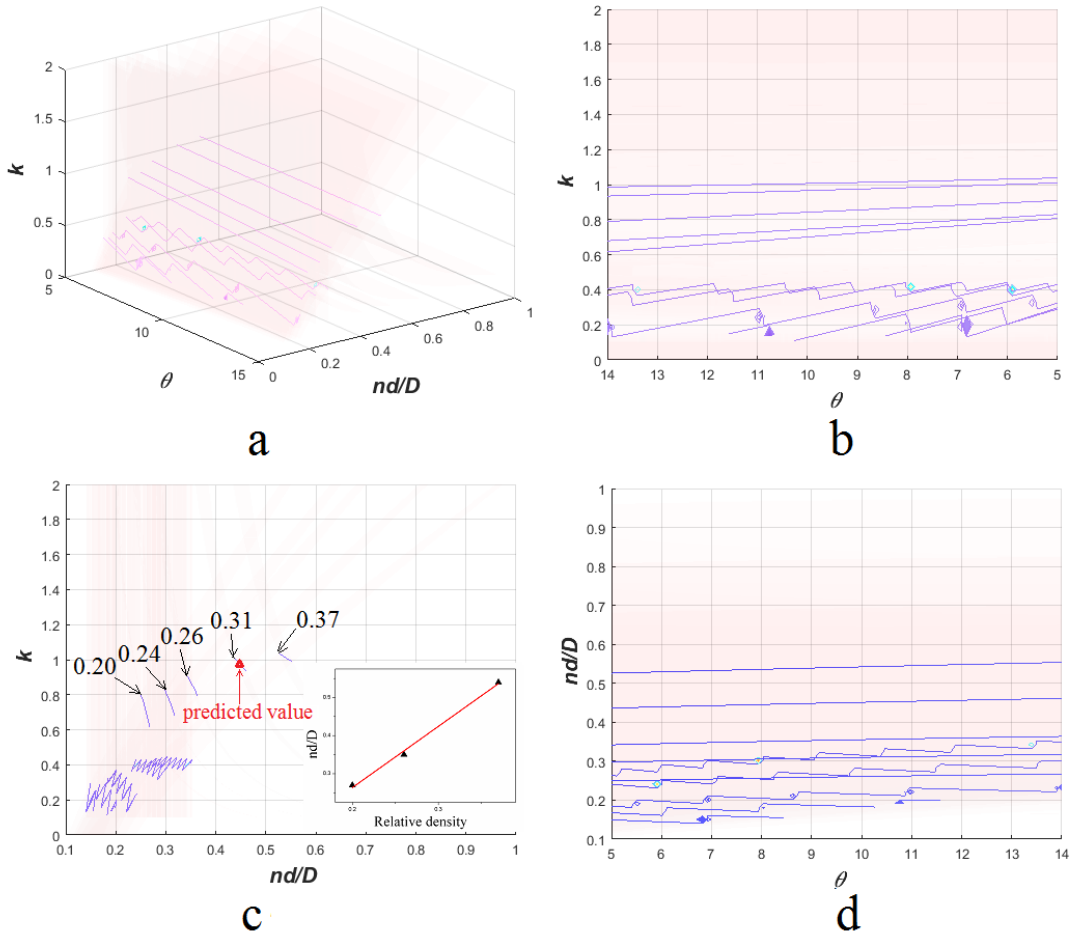

Fig. 16. The compatibility conditions of the geometrical characteristics of the lapping networks with relative densities: 0.24, 0.26, 0.31 and 0.37. Figures b, c and d are the three views of figure a.

For MFSSs with different relative densities, the compatibility condition of the geometrical characteristics changes with increasing the relative density. The coefficients k and nd/D of MFSSs with larger relative density is larger than that with lower relative density as shown in Fig. 16 (c). In addition, k becomes more and more insensitive to θ with the increase of the relative densities. In contrast to this, nd/D is not associated with θ. In fact, both of k and θ have effect on the relative density of the material, when the relative density is fixed. There will be a relation between k and θ, which has been shown in Fig. 16 (b) and explained by Eq. 11. By fitting the available results in Fig. 16 (c), the predicted value of the invariants k and nd/D can be obtained. Furthermore, the yield strength of MFSSs with other relative density will be calculated by solving Eq. 12. For example, fixing the value of θ as 10º, the available results of the

relative densities 0.2, 0.26 and 0.37 are used to fit the relation between the value of the relative density and the parameter *nd*/*D* as shown in the lower right corner of Fig. 16 (c). The equation of the fitting line is:

$$\frac{nd}{D} = 1.621\rho_r - 0.059 \tag{16}$$

The value of *k* for the relative density 0.31 is 0.4435. The yield stress for the relative density 0.31 can be obtained by substituting the values of *nd*/*D* and *k* into Eq.12. If the value of θ is unfixed, the value range of the yield stress for the relative density 0.31 is:

$$11.38\text{MPa} \le \sigma_{MFSS}^{0.31} \le 14.74\text{MPa} \tag{17}$$

Actually, the experimental result of the yield stress of the MFSSs with relative density 0.31 is 13.7MPa. The error is smaller than 15%.

The strain of MFSSs measured in the experiments is actually the strain of the whole structure. It is assumed that for the loose structure, the strain rate effect of MFSSs depends on the strain rate effect of the raw material 316L stainless steel. The strain of the structure mainly derives from the bending deflection at the fiber ends. The strain of the raw material is mainly the normal strain caused by the axial force in the fibers and the bending normal stress. The ratio of the strain rate of the fibers to that of the whole structure under the same compressive load is derived as follows:

$$\begin{aligned}\varepsilon_{fiber} &= \frac{24M}{Ek\pi d^3} + \frac{F\left(\sin\theta + K\cos\theta\right)}{EA} \\ &= \frac{F}{E}\left(\frac{\sin\theta + K\cos\theta}{A} + \frac{24l''\left(\cos\theta - K\sin\theta\right)}{k\pi d^3}\right)\end{aligned} \tag{18}$$

$$\varepsilon_{structure} = \frac{Fl''^2}{3EI_{type2}\sin\theta\cos\theta} = \frac{F}{E}\frac{64l''^2}{3\pi d^4\sin\theta\cos\theta} \tag{19}$$

$$\begin{aligned}\frac{\dot{\varepsilon}_{fiber}}{\dot{\varepsilon}_{structure}} &= \frac{\varepsilon_{fiber}}{\varepsilon_{structure}} \\ &= \frac{9}{2}\frac{nd}{D}\frac{\left(\cos\theta - K\sin\theta\right)\sin\theta\cos^2\theta}{k} \\ &\quad +3\left(\frac{nd}{D}\right)^2\left(\sin\theta + K\cos\theta\right)\sin\theta\cos^3\theta\end{aligned} \tag{20}$$

The relation between the strain rate effect of MFSSs and the strain rate effect of the raw material has been given in Eq. 20. The yield strengths of MFSSs under compressive

load at different strain rates are listed in Tab. 3. The scale factors of the yield strength corresponding to different strain rates are shown in Fig. 17. The scale factor is the ratio of the flow stress at a high strain rate to the quasi-static flow stress. Theoretical scale factor is derived based on the plastic kinematic model's factor, which scales the yield strength at a high strain rate. The theoretical results agree well with the experimental results for the MFSSs with the relative densities under 0.26, so the assumption that the strain rate effect of MFSSs depends on the strain rate effect of the raw material 316L stainless steel is validated. It can be observed in Fig.17 that the current theoretical model can effectively predict the strain rate effect of MFSSs with small relative densities.

Table 3. The yield strength of MFSSs with different relative densities at elevated strain rates

Relative density	0.001/s (MPa)	1100/s (MPa)	1500/s (MPa)	2000/s (MPa)
0.2	2.5	7.5	-	-
0.24	4	9.5	-	12.7
0.26	6	14	-	-
0.31	13.7	20	-	-
0.37	21	35	52	-

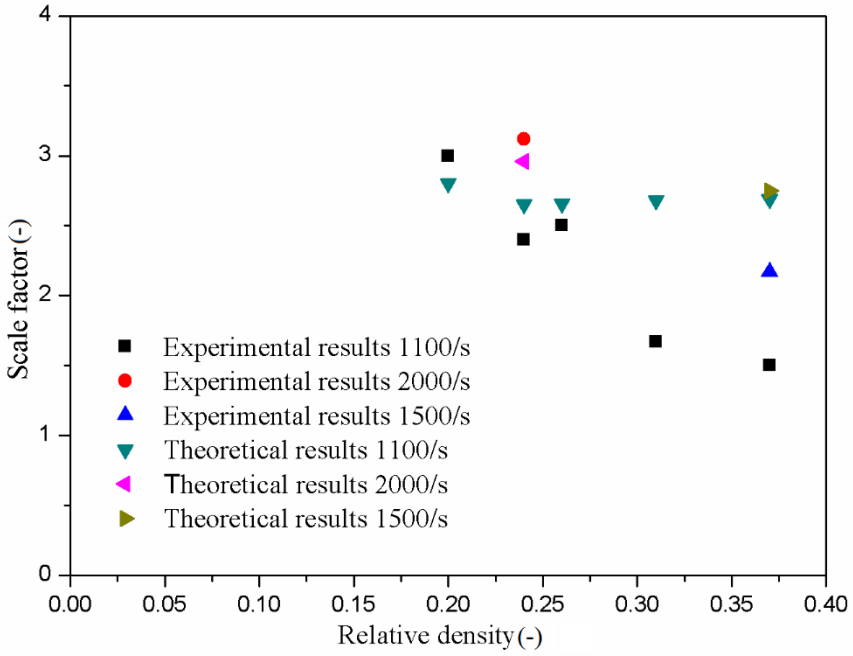

Fig. 17. The comparison between experimental and theoretical scale factors.

In summary, the regularization of MFSSs is effective in terms of the characterization of the compatibility condition of the geometrical characteristics and the prediction of the yield strength of MFSSs at different strain rates.

4.4 Analysis of strain field

At the strain rate of 1100/s, notable inertial effect can be observed from DIC in the specimen in Fig. 18. The values in the strain field vary from layer to layer regularly along the loading direction. The camera type is FASTCAM SA5 model 1000K-M1 and the record rate (fps) is 50000. The stress wave propagates in the specimen from the left interface and reflects at the right interface. In Fig. 18 (a), after the stress wave propagated in the specimen, the deformation of the regions near the incident bar occurs earlier than that of the regions near the transmission bar. It can be explained that the strain of the point 1 is larger than that of the point 2 marked by a red circle. In Fig. 18 (b), the stress wave reflects at the interface between the specimen and the transmission bar as a compressive wave. The strain of the point 2 becomes larger than that of the point 1 reversely. When the reflected wave reaches the left interface, the primary loading ends. Meanwhile, the speed of the specimen is approximately 0 and there is nearly no stress in the specimen, because the specimen is far softer than bar. That is why there is a plateau stage after No. 72 image. Choosing the sampling point far from the left interface, more data will be provided in the curve partly shown in Fig. 19.

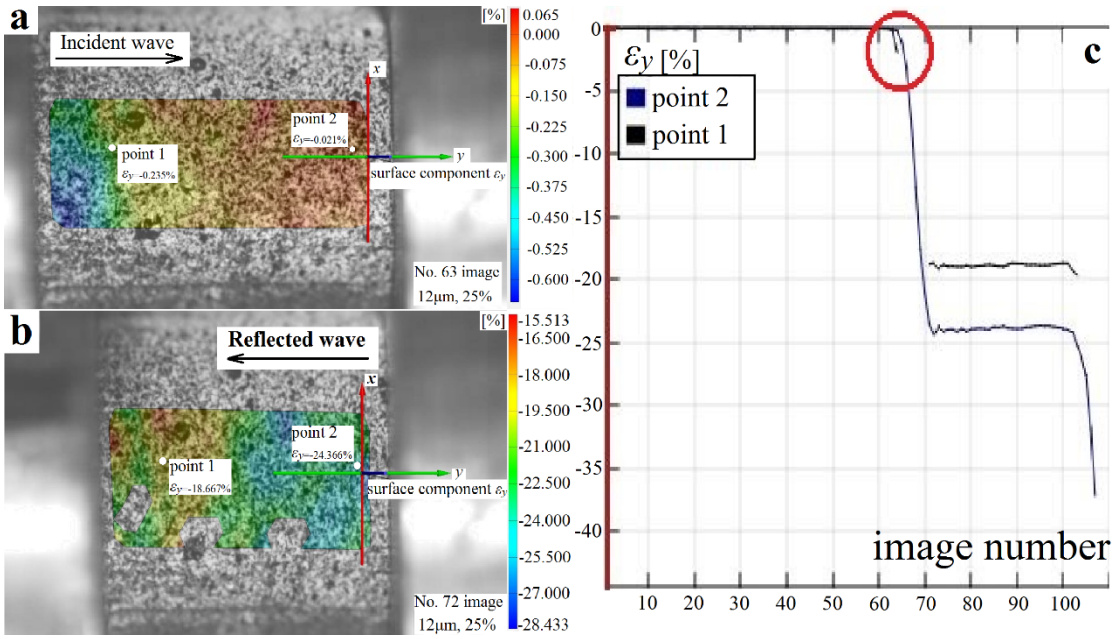

Fig. 18. The DIC results of specimen in SHPB test, in the picture the incident bar is on the left: a. No. 63 image, this state is marked in figure c with a red circle, the right figure presents strain versus number of pictures; b. No. 72 image, the stress wave reflects at the right interface.

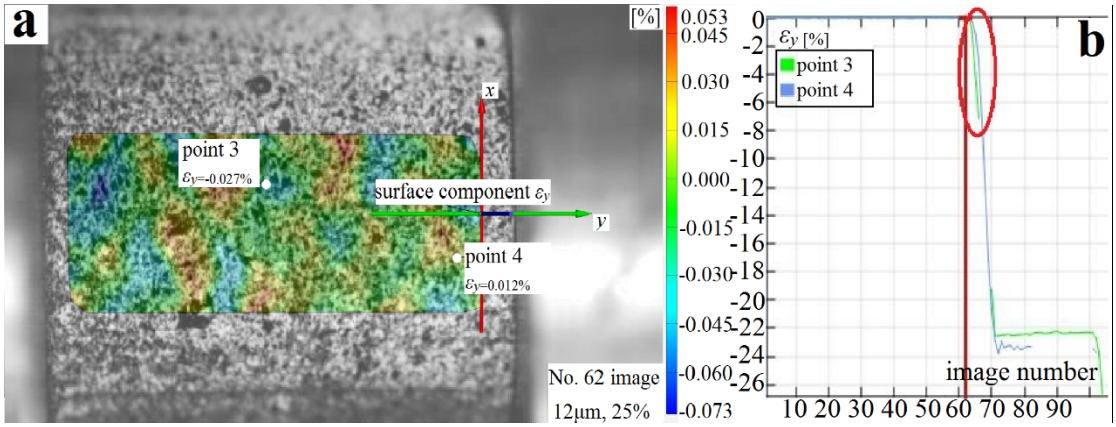

Fig. 19. Compared with the Fig. 18 more data will be obtained when the sampling point is far from incident bar.

The strain plateau of the right point is lower than that of the left point in Fig. 18 or Fig. 19, which means that the absolute strain value of the right point is higher than that of the left point. Furthermore, the absolute stress value of the part far from the loading end is higher than that of the part near the loading end, when the primary loading ends. The deformation occurs mainly at the part far from the loading end. To explain this

phenomena, the propagation process of the stress wave in the material will be studied. Firstly, based on the above-mentioned results, MFSSs can be reasonably assumed as a kind of elastic-plastic material with a decreasing strain hardening rate. The stress-strain relationship of the material satisfies the following inequality:

$$\frac{\mathrm{d}^2\sigma}{\mathrm{d}\varepsilon^2} < 0 \tag{21}$$

Under a step load, the stress wave in MFSSs is a weak discontinuity wave. Let the wave propagate from x=0 rightwards and reflect at two rigid walls. The x-t graph of this weak discontinuity wave gives the distribution characteristics of the physical quantities v, σ, ε. These physical quantities without regard to energy on both sides of the characteristic line presented in Fig. 20 (a) meet the conservation conditions:

$$\begin{cases} \mathrm{d}v = \mp C\mathrm{d}\varepsilon \\ \mathrm{d}\sigma = \mp\rho_0 C\mathrm{d}v \end{cases} \tag{22}$$

Eq. 22 is the formula for the weak discontinuity wave front.

$$\begin{cases} [v] = \mp C[\varepsilon] \\ [\sigma] = \mp\rho_0 C[v] \end{cases} \tag{23}$$

Eq. 23 is the formula for the strong discontinuity wave front, where C is the speed of stress wave. ρ_0 is MFSSs density. "-" corresponds to the right-traveling wave and "+" corresponds to the left-traveling wave.

Based on the stress wave theory, the regions separated by heavy lines can be divided into three types: (0, 2, 9), (1, 5, 6, 10, 13) and (3, 4, 7, 8, 11, 12, 14). 0, 2, 9 are regions with constant value and 1, 5, 6, 10, 13 are regions with simple waves, in which the value of the physical quantity increases or decreases monotonically along the across characteristic line direction. 3, 4, 7, 8, 11, 12, 14 are regions consisting of Picard mixed problem regions (4, 7, 11, 12) and Darboux boundary value problem regions (3, 8, 14). The numerical solution of these two problem regions has been explored on the propagation of plastic waves in tension specimens of finite length [26]. As shown on the right side of Fig. 20 (b) (c) (d), three typical states can be found at the points of time t_1, t_2 and t_3, respectively. These three states are correspond to the three states captured by DIC processing shown on the left side of Fig. 20 (b) (c) (d), respectively. At t_1 the strain field of the material can be divided into 2, 1, 0 three regions. The strain in region

0 is constant 0. In region 1, the strain decreases monotonically along the propagation direction, and in region 2, it is constant. The DIC results show that the strain on the left part corresponding to region 2 is not a constant, because the left sampling point is not completely on the load end and the speed of the last plastic wave is much slower than that of the elastic wave. In the sampling time, the plastic wave front has not arrived at the sampling point. In fact, in consideration of the effect of the plastic waves, the increment of the strain is larger than 3.1%, which can be verified by the first equation in Eq. 22. The two probable speeds of the elastic wave in MFSSs are measured by the delay of the signal of the transmitted wave relative to the signal of the reflected wave and calculated by the following equation:

$$C_0 = \sqrt{E/\rho_0} \tag{24}$$

where C_0 is the elastic wave speed. E is the Young modulus of MFSSs. ρ_0 is the density of MFSSs. The unloading wave doesn't appear in Fig. 20 (a), because the duration of elastic disturbance is 160μs (800mm/5000m/s) and this time point is too late to be included in Fig. 20 (a). 800mm is twice the length of the striker bar. 5000m/s is the stress wave speed in steel SHPB. The disturbance velocity at the load end is 12m/s. At time t_2, the strain field can be divided into 2, 5, 3 and 4 corresponding to Fig. 20 (c). For the state shown in Fig. 20 (d), t_3 falls in between I consisting of 11, 8, 6, 9 and II consisting of 7, 8, 6, 4. The values (-21.6% and -23.1%) of the strain at both side of the strain field are very close, so the stress values at both side of the sampling area are nearly same. Because the primary loading ends around t_3, the stress concentration will occur at the place, where ε is equal to -24.6% as shown in Fig. 20 (d). Generally speaking, the distribution of the strain in the experiments agrees with the theoretical solution.

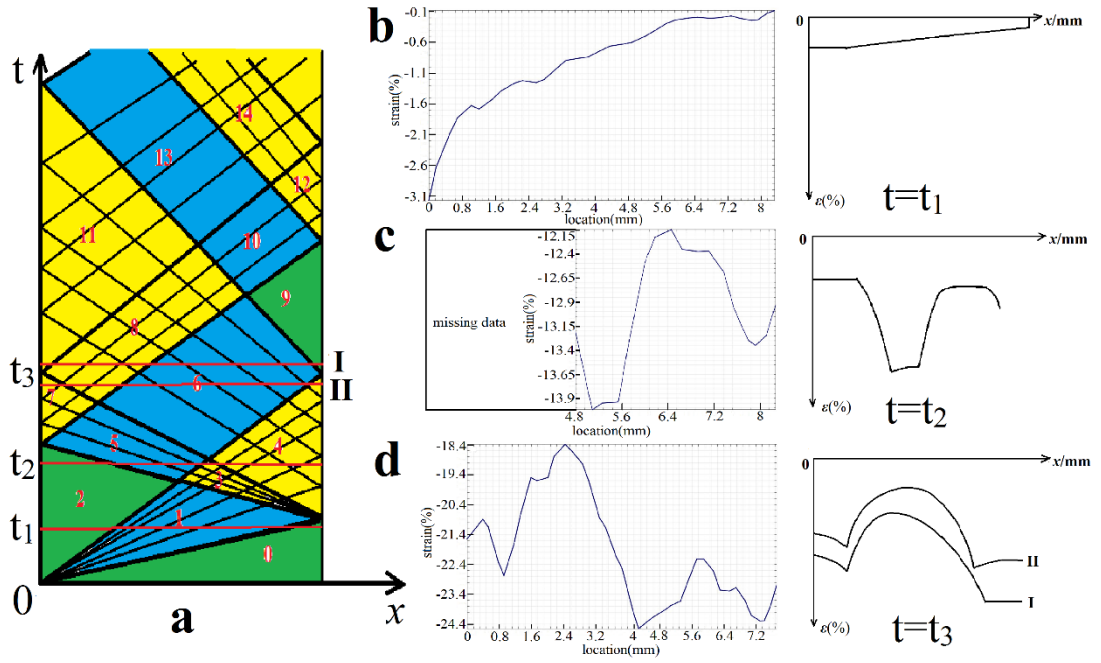

Fig. 20. The schematic propagation of a weak discontinuity wave: a. the *x*-t graph of the weak discontinuity wave propagating from *x*=0. Green region consists of three constant stress regions. Blue region consists of five simple wave regions. Yellow region consists of seven complex wave regions. Figures b, c and d present the *ε*-*x* graphs of the stress wave in specimen (left) and theoretically (right) at the timings t_1, t_2 and t_3, respectively.

The deformation mode observed in Fig. 18 is not a shock wave mode [27], because the MFSSs doesn't collapse layer-by-layer apparently. At the loading speed of 12m/s, the area of the stress concentration locates at the part far from the load end (called lower speed mode), but it can be also assumed that the deformation mode will change with increasing the loading speed. When the loading speed is higher than a speed (the critical speed), MFSSs will deform in shock wave mode. To prove this presumption, a power-law hardening (PLH) idealized model [27] is adopted to fit the constitutive behavior of MFSSs. Based on PLH model, several plastic wave fronts are reasonably simplified as a single first-order singular surface. Then, there are only two strong discontinuity wave fronts propagating in MFSSs. The state parameters before elastic wave front (v_0, σ_0, ε_0), after elastic wave front (v', σ', ε') and after plastic wave front (v_1, σ_1, ε_1) are defined in Appendix C. Variables v, σ, ε are the particle velocity, the stress and the strain, respectively. The values of v_0, σ_0 and ε_0 are equal to 0. Taking the conservation

condition of the mass and moment into consideration, the relations among these three sets of variables are achieved:

$$\text{for A} \begin{cases} [v] = -C_0 [\varepsilon] \\ [\sigma] = -\rho_0 C_0 [v] \end{cases} \tag{25}$$

$$\text{for B} \begin{cases} [v] = -C_1 [\varepsilon] \\ [\sigma] = -\rho_0 C_1 [v] \end{cases} \tag{26}$$

where C_1 is the speed of plastic wave front. Then the relations can be derived:

$$\text{for A} \begin{cases} v' = C_0 \varepsilon' \\ \sigma' = \rho_0 C_0 v' \end{cases} \Rightarrow \sigma' \varepsilon' = \rho_0 v'^2 \tag{27}$$

$$\text{for B} \begin{cases} v_1 - v' = -C_1 (\varepsilon_1 - \varepsilon') \\ \sigma_1 - \sigma' = -\rho_0 C_1 (v_1 - v') \end{cases} \Rightarrow (\sigma_1 - \sigma')(\varepsilon_1 - \varepsilon') = \rho_0 (v_1 - v')^2 \tag{28}$$

Because in the region between the elastic wave front and the plastic wave front, stress σ' is the yield strength σ_y, strain ε' is the strain corresponding to the yield strength ε_e, so:

$$\varepsilon_1 - \varepsilon_e = \varepsilon_p \tag{29}$$

$$\sigma_y \varepsilon_e = \rho_0 v'^2 \tag{30}$$

$$(\sigma_1 - \sigma_y) \varepsilon_p = \rho_0 (v_1 - v')^2 \tag{31}$$

where ε_p is the plastic strain. A PLH model considering a regulation term is employed:

$$\sigma_1 (\varepsilon_p) = \sigma_y + j\varepsilon_p + x\varepsilon_p{}^q \tag{32}$$

where j, x and q are the first order strength index, high order strength index and strain hardening index, respectively. Variables j, x and q can be obtained by fitting the results of quasi-static experiments as shown in Fig. 21. Substituting Eq. 32 into Eq. 31, the relation between plastic strain and particle speed can be derived as:

$$v_1 - v' = \sqrt{\frac{j\varepsilon_p^2 + x\varepsilon_p{}^{q+1}}{\rho_0}} \tag{33}$$

When strain ε_1 reaches the densification strain ε_d, the speed increment is treated as the critical speed v_c [27, 28]. Here, taking the elasticity modulus of MFSSs as the standard, when the hardening modulus is equal to the elasticity modulus, it can be thought of as the initial point of densification. Namely:

$$E_e = E_y = \frac{d\sigma_1(\varepsilon_p)}{d\varepsilon_p} = j + qx\varepsilon_p^{q-1} \tag{34}$$

where E_e and E_y are the elasticity modulus and the hardening modulus, respectively. By solving the Eq. 34 and Eq. 29, ε_d=0.41 is obtained. Substituting ε_p=0.36 into Eq. 33, the critical speed can be derived as:

$$v_c = v' + 55\text{m/s} \tag{35}$$

The value of v' can be obtained from Eq. 27: v'=15m/s, so the critical speed is 70m/s.

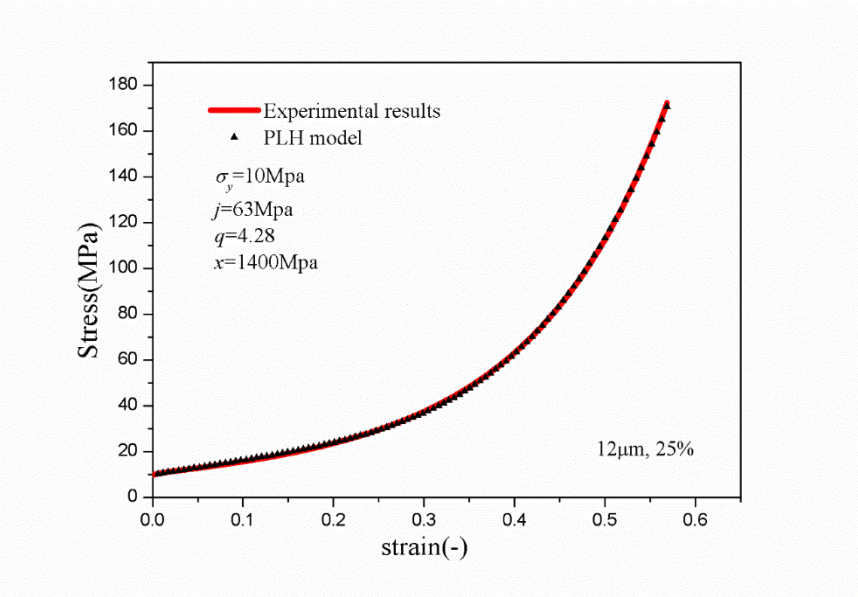

Fig. 21. Due to the existence of the regulation term, fitting curve agrees well with the quasi-static test results. For the stress- strain curve of MFSSs in 12μm fiber diameter and 25% relative density, ε_e is 5%.

Two different deformation modes of MFSSs at three loading speeds of 12m/s, 60m/s and 75m/s are shown in Fig. 22. At the speed of 12m/s, the stress concentration locates at the lower half of the FE model, which has been explained above. At the speed of 60m/s, the mode is a transition stage (a state falls in between the mode at a low speed like 12m/s and the mode at the high speed over 70m/s). There are two stress concentration zones at these two places. At the speed of 75m/s, the deformation accompanies with the stress wave. There is only one apparent stress concentration zone at the load end, while the stress concentration caused by the superposition of the stress waves occurs later and is not remarkable. Thus, with the increase of the loading speed,

the deformation mode of MFSSs will change. When the loading speed surpasses 70m/s, MFSSs will deform layer by layer, which demonstrate that the theoretical critical speed is reliable.

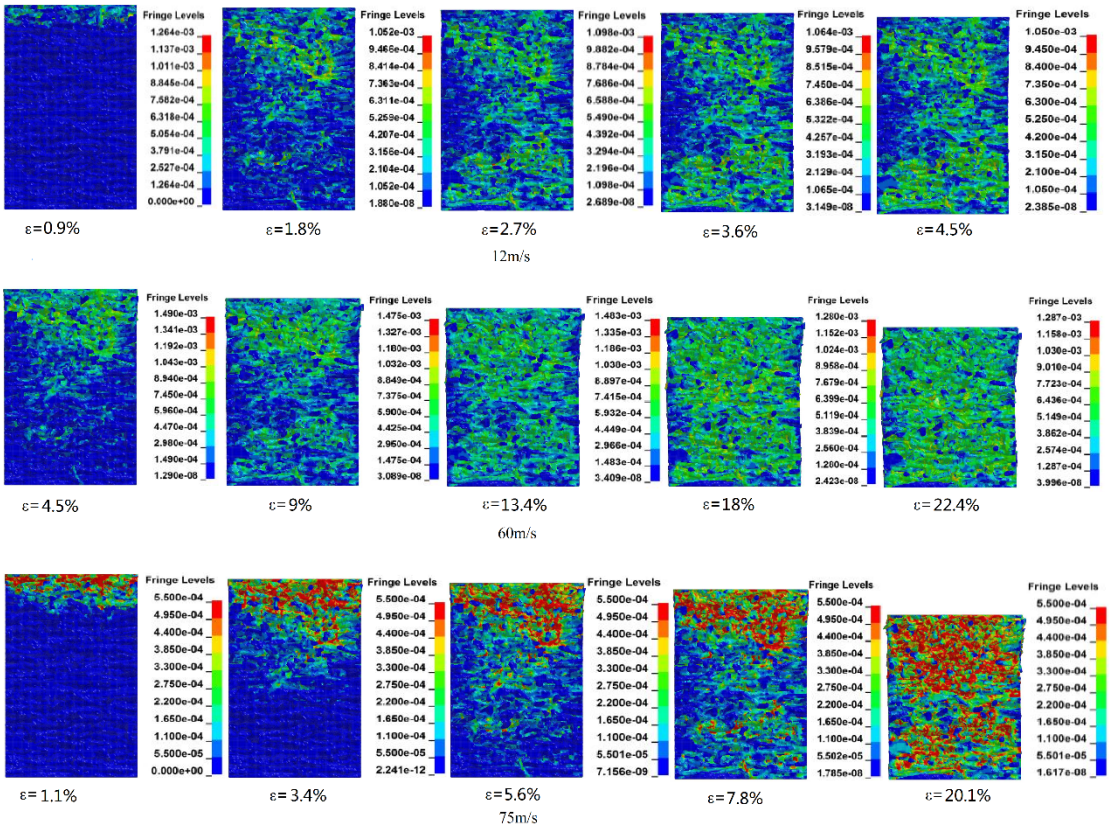

Fig. 22. The deformation modes of MFSSs bearing the load at speed of 12m/s, 60m/s and 75m/s, respectively. The FE model is 1340μm high. The area of stress concentration is shown in Von Mises effective stress distribution (MPa).

5. Conclusion

The compressive mechanical behaviors of MFSSs at different strain rates are investigated and the influence of the relative density and strain rate on the mechanical property of MFSSs is examined. Based on experimental results, FEM model generated by 3D reconstruction technique and an idealized model are proposed to describe the mechanical performance of MFSSs. An idealized lapping network is introduced to study the topological invariants of MFSSs and to predict the compressive yield strength of MFSSs at different strain rates. The propagation of stress wave in MFSSs is explored

and a critical speed for shock wave mode is derived. Some conclusions are drawn as follows:

(1) The yield strength of MFSSs increases with the increase of the relative densities and loading strain rates.

(2) Both the randomly generated idealized model and FEM model generated by 3D reconstruction technique are practical in simulating the mechanical response of MFSSs.

(3) The strain rate effect and the yield strength of MFSSs depend on the topological invariants of MFSSs' structure. The yield strength of MFSSs with different relative densities can be precisely predicted by the proposed lapping network.

(4) There are two speed-dependent deformation modes of MFSSs: lower speed mode and shock wave mode.

6. Appendix A

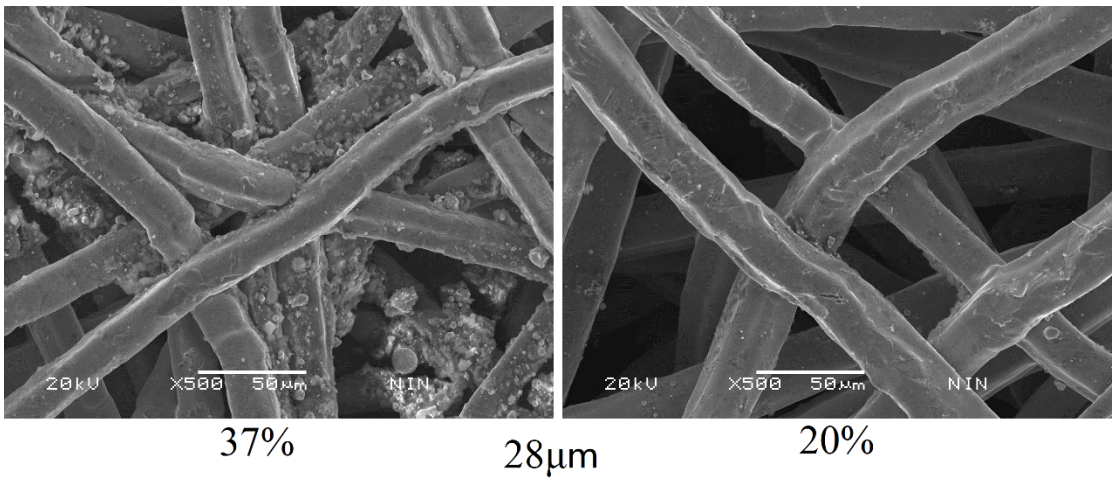

Fig. A. Comparison between the internal morphology of MFSSs with 37% relative density and 20% relative density.

Appendix B

F is the component force of the total force applied on the top surface of the structure. l'' is half of l'. F_j is the reaction force from the symmetric part of the fiber. M is the bending moment at the bonding point. The expression of F is Eq.1. When F is applied, the displacement of fiber end along F is a composition of the deflection of fiber end (Eq. 3) and the reduced length of fiber (Eq. 4). The deformation compatibility condition

is given in Eq. 5.

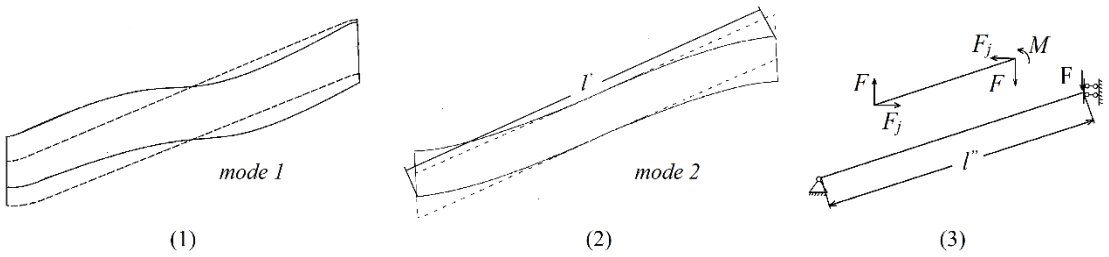

Fig. B. The deformation mode and the free-body diagram of fibers under compressive load in the model.

$$F = \frac{F_{\Sigma}}{2n^2} \tag{1}$$

$$l'' = \frac{l'}{2} \tag{2}$$

$$w = \frac{\left(F\cos\theta - F_j \sin\theta\right) l''^3}{3EI} \tag{3}$$

$$\Delta l'' = \frac{\left(F\sin\theta + F_j \cos\theta\right) l''}{EA} \tag{4}$$

$$\frac{w}{\Delta l''} = \cot\theta \tag{5}$$

The relation between F and F_j can be obtained by substituting Eq. 3 and Eq. 4 into Eq. 5. The expression is Eq. 6. The coefficient of F is represented by K for simplicity.

$$F\cos\theta\left(1 - \frac{3d^2}{16l''^2}\right)\frac{16l''^2\sin\theta}{16l''^2\sin^2\theta + 3d^2\cos^2\theta} = F_j \tag{6}$$

$$FK = F_j \tag{7}$$

$$l' = \frac{D}{2n\cos\theta} = \frac{l}{2n} \Rightarrow l = \frac{D}{\cos\theta} \tag{8}$$

Substituting Eq. 8 and Eq. 2 into Eq. 6 the expression of K can be written as Eq. 9:

$$K = \left[1 - 3\left(\frac{nd}{D}\right)^2 \cos^2\theta\right]\frac{\tan\theta}{\tan^2\theta + 3\left(\frac{nd}{D}\right)^2 \cos^2\theta} \tag{9}$$

The expression of the bending moment M is Eq. 10.

$$M = \left(F\cos\theta - F_j \sin\theta\right) l'' \tag{10}$$

Two fiber cross-section types at bonding point are considered. It is assumed that the fiber cross-section at bonding point is pressed or melts approximately into a rectangle (length b and width $k \times d$, k: see Fig. 12) during processing. This is one shape type. Another one is the original circular cross-section. The inertia moments of these two cross-section types are expressed in Eq. 12 and Eq. 13.

$$\frac{\pi d^2}{4} = kdb \Rightarrow b = \frac{\pi d}{4k} \tag{11}$$

$$I_{type1} = \frac{k^2 d^4}{48} \tag{12}$$

$$I_{type2} = \frac{\pi d^4}{64} \tag{13}$$

The maximum normal stress in fiber is derived as Eq. 14.

$$\sigma_{\max} = \begin{cases} \dfrac{24M}{k\pi d^3} + \dfrac{F\sin\theta + F_j\cos\theta}{A} & \text{cross-section type 1} \\ \quad or & \\ \dfrac{32M}{\pi d^3} + \dfrac{F\sin\theta + F_j\cos\theta}{A} & \text{cross-section type 2} \end{cases} \tag{14}$$

When the structure yields, the nominal stress of the structure is σ_{yMFSS} and the maximum normal stress in fiber reaches σ_{y316L}, which has been expressed in Eq. 15 and Eq. 16.

$$F_{\Sigma} = D^2\sigma_{yMFSS} \Rightarrow F = \frac{D^2\sigma_{yMFSS}}{2n^2} \tag{15}$$

$$\sigma_{\max} = \sigma_{y316L} \tag{16}$$

Then for cross-section type 1 the Eq. 14 can be rewritten as Eq. 17 or Eq. 18. For cross-section type 2 it can be written as Eq. 19.

$$\frac{\sigma_{y316L}}{\sigma_{yMFSS}}\left(\frac{nd}{D}\right)^3 = \left[\frac{3(\cos\theta - K\sin\theta)}{k\pi\cos\theta} + \frac{nd}{D}\frac{4(\sin\theta + K\cos\theta)}{\pi}\right] \tag{17}$$

$$k = \frac{3(\cos\theta - K\sin\theta)}{\pi\cos\theta} \Bigg/ \left[\frac{\sigma_{y316L}}{\sigma_{yMFSS}}\left(\frac{nd}{D}\right)^3 - \frac{nd}{D}\frac{4(\sin\theta + K\cos\theta)}{\pi}\right] \tag{18}$$

$$\left[\frac{\sigma_{y316L}}{\sigma_{yMFSS}}\left(\frac{nd}{D}\right)^3 - \frac{nd}{D}\frac{4(\sin\theta + K\cos\theta)}{\pi}\right] = \frac{4(\cos\theta - K\sin\theta)}{\pi\cos\theta} \tag{19}$$

$$k = \frac{1}{4\cos\theta}\left(\frac{nd}{D}\frac{\pi}{\rho_r} - 2\sin\theta\frac{D}{nd}\right) \tag{20}$$

The compatibility conditions of geometrical characteristics will be obtained by solving two simultaneous equations Eq. 18 and Eq. 20 or Eq. 19 and Eq. 20. Solutions in different conditions have been plotted in Fig. 15 and Fig. 16. The solution of Eq. 18 and Eq. 20 will be discussed in the text.

Appendix C

In Fig. C **A** and **B** are elastic wave front and plastic wave front, respectively. **A** corresponds to the characteristic line e and **B** corresponds to the characteristic line p as shown in Fig. C (c).

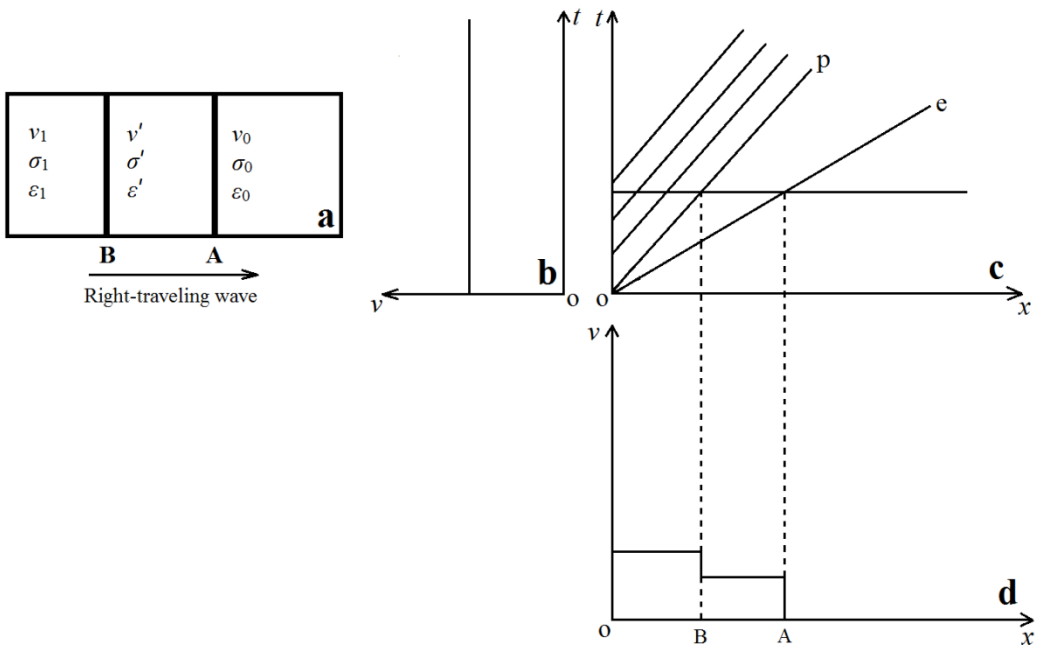

Fig. C. Two strong discontinuity wave front propagate in material: a. physical quantities on each side of the stress wave front; b. the t-v graph of step load; c. the x-t graph of the stress waves; d. PLH model is a constitutive model with increasing strain hardening rate in plastic range, so its stress wave front is a single first-order singular surface.

7. Acknowledgements

The author acknowledges the financial support of the National Key R&D Program of China (2016YFC0801200), the National Natural Science Foundation of China

(11672043, 11732003, 11802028), the Opening Project of State Key Laboratory for Strength and Vibration of Mechanical Structures (SV2019-KF-02), the Opening Project of State Key Laboratory of Traction Power (TPL1701), Project funded by China Postdoctoral Science Foundation (2018M640072), the Project of State Key Laboratory of Explosion Science and Technology (YBKT18-07, KFJJ19-12M) and other projects of China (614260601010617 and SAST2017-029).

References

[1] Yuranov I, Kiwi-Minsker L, Renken A. Structured combustion catalysts based on sintered metal fiber filters. APPL CATAL B-ENVIRON. 2003; 43: 217-227. https://doi.org/10.1016/S0926-3373(02)00304-1

[2] Chadwick C. Nuclear power generation: improving HEPA filter trains through effective pre-filtration. FILTR SEPARAT. 2010; 47: 18-20. https://doi.org/10.1016/S0015-1882(10)70260-3

[3] Golosnoy IO, Tan JC, Clyne TW. Ferrous Fibre Network Materials for Jet Noise Reduction in Aeroengines Part I: Acoustic Effects. ADV ENG MATER. 2008; 10: No. 3. DOI: 10.1002/adem.200700303

[4] Zou SP, Wan ZP, Lu LS, Tang Y. Bending behavior of porous sintered stainless steel fiber honeycombs. J MATER ENG PERFORM. 2017; 26: 744-751. DOI: 10.1007/s11665-016-2452-2

[5] Borodulina S, Motamedian HR, Kulachenko A. Effect of fiber and bond strength variations on the tensile stiffness and strength of fiber networks. INT J SOLIDS STRUCT. 2016; 000: 1-14. https://doi.org/10.1016/j.ijsolstr.2016.12.013

[6] Sabuncuoglu B, Acar M, Silberschmidt VV. A parametric finite element analysis method for low-density thermally bonded nonwovens. COMP MATER SCI. 2012; 52: 164-170. https://doi.org/10.1016/j.commatsci.2010.12.005

[7] Sabuncuoglu B, Acar M, Silberschmidt VV. Finite element modelling of fibrous networks: Analysis of strain distribution in fibers under tensile load. COMP MATER SCI. 2013; 79: 143-158. https://doi.org/10.1016/j.commatsci.2013.04.063

[8] Li DT, Xia W, Fang QZ, Yu WS, Shen SP. Experimental and numerical investigations on the tensile behavior of 3D random fibrous materials at elevated temperature. COMPOS STRUCT. 2017; 160: 292-299. https://doi.org/10.1016/j.compstruct.2016.10.075

[9] Kim OV, Litvinov RI, Weisel JW, Alber MS. Structural basis for the nonlinear mechanics of fibrin networks under compression. BIOMATERIALS. 2014; 35: 6739-6749. https://doi.org/10.1016/j.biomaterials.2014.04.056

[10] Markaki AE, Clyne TW. Mechanics of thin ultra-light stainless steel sandwich sheet material: Part I. Stiffness. ACTA MATER. 2003; 51: 1341-1350. DOI: 10.1016/s1359-6454(02)00528-1

[11] Wilbrink DV, Beex LAA, Peerlings RHJ. A discrete network model for bond failure and frictional sliding in fibrous materials. INT J SOLIDS STRUCT. 2013; 50: 1354-1363. https://doi.org/10.1016/j.ijsolstr.2013.01.012

[12] Liu JX, Chen ZT, Wang H, Li KC. Elasto-plastic analysis of influences of bond deformability on the mechanical behavior of fiber networks. Theor Appl Fract Mech. 2011; 55: 131-139. DOI: 10.1016/j.tafmec.2011.04.003

[13] Kirkayak L. Strain rate effects on compressive behavior of covalently bonded CNT networks. PHYSICA E. 2016; 80: 168-175. https://doi.org/10.1016/j.physe.2016.02.004

[14] Andersen O, Vesenjak M, Fiedler T, Jehring U, Krstulovič-Opara L. Experimental and Numerical Evaluation of the Mechanical Behavior of Strongly Anisotropic Light-Weight Metallic Fiber Structures under Static and Dynamic Compressive Loading. MATERIALS. 2016; 9: 398. DOI: 10.3390/ma9050398

[15] Dean J, S-Fallah A, Brown PM, Louca LA, Clyne TW. Energy absorption during projectile perforation of lightweight sandwich panels with metallic fiber cores. COMPOS STRUCT. 2011; 93: 1089-1095. https://doi.org/10.1016/j.compstruct.2010.09.019

[16] Karakoç A, Hiltunen E, Paltakari J. Geometrical and spatial effects on fiber network connectivity. COMPOS STRUCT. 2017; 168: 335-344. https://doi.org/10.1016/j.compstruct.2017.02.062

[17] Jin MZ, Chen CQ, Lu TJ. The mechanical behavior of porous metal fiber sintered sheets. J MECH PHYS SOLIDS. 2013; 61: 161-174. https://doi.org/10.1016/j.jmps.2012.08.006

[18] Silberstein MN, Pai C, Rutledge GC, Boyce MC. Elastic-plastic behavior of non-woven fibrous mats. J MECH PHYS SOLIDS. 2012; 60: 295-318. https://doi.org/10.1016/j.jmps.2011.10.007

[19] Ridruejo A, González C, LLorca J. A constitutive model for the in-plane mechanical behavior of nonwoven fabrics. INT J SOLIDS STRUCT. 2012; 49: 2215-2229. https://doi.org/10.1016/j.ijsolstr.2012.04.014

[20] Zhao TF, Chen CQ, Deng ZC. Elastoplastic properties of transversely isotropic sintered metal fiber sheets. MAT SCI ENG A-STRUCT. 2016; 662: 308-319. DOI: 10.1016/j.msea.2016.03.085

[21] Veyhl C, Fiedler T, Jehring U, Andersen O, Bernthaler T, Belova IV, Murch GE. On the mechanical properties of sintered metallic fibre structures. MAT SCI ENG A-STRUCT. 2013; 562: 83-88. https://doi.org/10.1016/j.msea.2012.11.034

[22] LS-DYNA Library.

[23] Cowper G, Symonds P. Strain hardening and strain-rate effects in the impact loading of cantilever beam, Tech. Rep., Brown University Division of Applied Mathematics, 1957.

[24] Wedberg D, Lindgren L. Modelling flow stress of AISI 316L at high strain rates. MECH MATER. 2015; 91: 194-207. http://dx.doi.org/10.1016/j.mechmat.2015.07.005

[25] Tan PJ, Reid SR, Harrigan JJ, Zou Z, Li S. Dynamic compressive strength properties of aluminium foams. Part I-experimental data and observations. J MECH PHYS SOLIDS. 2005; 53:2174-2205. https://doi.org/10.1016/j.jmps.2005.05.007

[26] Karman TV, Bohnenblust HF, Hyers DH. The Propagation of Plastic Waves in Tension Specimens of Finite Length. Theory and Methods of Integration. NDRC Report A-103, 1942; PB. 18477.

[27] Zheng ZJ, Yu JL, Li JR. Dynamic crushing of 2D cellular structures: a finite element study. INT J IMPACT ENG. 2015; 32: 650-664. https://doi.org/10.1016/j.ijimpeng.2005.05.007

[28] Xiao LJ, Song WD, Wang C, Tang HP, Fan QB, Liu N, Wang J. Mechanical properties of open-cell rhombic dodecahedron titanium alloy lattice structure manufactured using electron beam melting under dynamic loading. INT J IMPACT ENG. 2017; 100: 75-89. https://doi.org/10.1016/j.ijimpeng.2016.10.006